Title: An altered cell-specific subcellular distribution of translesion synthesis DNA polymerase kappa (POLK) in aging neurons

Authors: Mofida Abdelmageed, Premkumar Palanisamy, Victoria Vernail, Yuval Silberman, Shilpi Paul, and Anirban Paul[#].

Corresponding author anirban@psu.edu

Affiliation: Neural and Behavioral Sciences Department, Penn State College of Medicine, Hershey, PA 17033

Abstract

Genomic stability is critical for cellular function, however, in the central nervous system highly metabolically active differentiated neurons are challenged to maintain their genome over the organismal lifespan without replication. DNA damage in neurons increases with chronological age and accelerates in neurodegenerative disorders, resulting in cellular and systemic dysregulation. Distinct DNA damage response strategies have evolved with a host of polymerases. The Y-family translesion synthesis (TLS) polymerases are well known for bypassing and repairing damaged DNA in dividing cells. However, their expression, dynamics, and role if any, in enduring postmitotic differentiated neurons of the brain are completely unknown. We show through systematic longitudinal studies for the first time that DNA polymerase kappa (POLK), a member of the Y-family polymerases, is highly expressed in neurons. With chronological age, there is a progressive and significant reduction of nuclear POLK with a concomitant accumulation in the cytoplasm that is predictive of brain tissue age. The reduction of nuclear POLK in old brains is congruent with an increase in DNA damage markers. The nuclear POLK colocalizes with damaged sites and DNA repair proteins. The cytoplasmic POLK accumulates with stress granules and endo/lysosomal

markers. Nuclear POLK expression is significantly higher in GABAergic interneurons compared to excitatory pyramidal neurons and lowest in non-neurons, possibly reflective of the inherent biological differences such as firing rates and neuronal activity. Interneurons associated with microglia have significantly higher levels of cytoplasmic POLK in old age. Finally, we show that neuronal activity itself can lead to an increase in nuclear POLK levels and a reduction of the cytoplasmic fraction. Our findings open a new avenue in understanding how different classes of postmitotic neurons deploy TLS polymerase(s) to maintain their genomic integrity over time, which will help design strategies for longevity, healthspan, and prevention of neurodegeneration.

Introduction

Throughout the organismal lifespan, continuous exposure to exogenous and endogenous agents can damage one or both strands of the DNA thus causing a persistent threat to genomic integrity (Iyama and Wilson 2013; Yan and Vaziri 2020; Chatterjee and Walker 2017; Tubbs and Nussenzweig 2017). Due to their long lifespan, increased transcriptional activity, and large energy demands, neurons are highly susceptible to cumulative DNA damage (Welch and Tsai 2022; Caldecott et al. 2022; Wu et al. 2021; Reid et al. 2021; Madabhushi et al. 2014). Neuronal genomic enhancer regions are hotspots for constant high levels of DNA single-strand breaks (SSBs) repair synthesis process, thus revealing that neurons are undergoing localized and continuous DNA breakage (Reid et al. 2021; Wu et al. 2021). In addition, the threat of genomic instability can also be contributed by normal “programmed” DNA breaks like topoisomerase-induced breaks for the removal of topological stress during transcription. High levels of such programmed DNA breakage occur in neurons, during development, differentiation, and maintenance (Caldecott et al. 2022). Recently, it was shown that programmed SSBs in the enhancer regions can be repaired by Poly(ADP-Ribose) Polymerase 1 (PARP1) and X-ray cross-complementing protein 1 (XRCC1)-mediated pathways (Wu et al. 2021). XRCC1 is a DNA repair scaffold protein that plays a role in

multiple repair pathways including base excision repair (BER) and single-strand break repair (SSBR) (London 2020). Due to high mitochondrial activity in the neurons, which consumes about 20% of the body's oxygen supply (Attwell and Laughlin 2001), neurons exhibit high levels of reactive oxygen species (ROS)-mediated DNA damage. ROS can damage DNA by oxidizing bases and creating abasic sites (Lindahl and Barnes 2000; Madabhushi et al. 2014; Tubbs and Nussenzweig 2017). One of the most common ROS-induced DNA modifications is 8-oxo-7,8-dihydroguanine (8oxo-dG) (Amente et al. 2019; Ding et al. 2017), a lesion that is often resolved through BER (Markkanen 2017). Unrepaired SSBs hinder transcription and can also lead to DSBs. A strong association exists between unrepaired DNA damage causing loss of genomic integrity with aging and neurodegeneration (Caldecott et al. 2022; Welch and Tsai 2022). Hence, survival strategies have evolved to preserve genomic stability through multiple DNA damage response (DDR) pathways allowing the neurons to function effectively. Impaired DDR leads to genomic instability triggering signaling cascades, stalling transcription, and creating mutagenesis, thus altering the cellular fate toward anomalous cell cycle activation, apoptosis, or senescence, which are hallmarks of aging and age-associated diseases (Hoeijmakers 2009; Madabhushi et al. 2014; Chow and Herrup 2015; McKinnon 2017; Tubbs and Nussenzweig 2017; Welch and Tsai 2022).

One unique mechanism that bypasses DNA adducts, synthesizes DNA past damage, and functions in post-replication DNA repair is through translesion synthesis (TLS) DNA polymerases (Sale et al. 2012; Gao et al. 2017; Powers and Washington 2018; Lehmann 2006; Paniagua and Jacobs 2023). TLS polymerases are well-studied in dividing cells, and the Y-family TLS polymerases include Rev1, Pol kappa (Polk), Pol iota (Poli), and Pol eta (Polh) (Guo et al. 2009; Sale et al. 2012; Vaisman and Woodgate 2017). However, their role in postmitotic cells is not explored. There is evidence of the role of POLK in dorsal root ganglion (DRG) neurons upon the treatment of genotoxic agents like cisplatin where POLK is upregulated (Zhuo et al. 2018) and is essential for efficiently and accurately repairing cisplatin crosslinks (Jha and Ling 2018). POLK

can perform error-free TLS across bulky DNA adducts at the N2 position of guanine induced by the genotoxic agent benzo[a]pyrene-dihydrodiol-epoxide (BPDE) and mitomycin C (Kanemaru et al. 2017; Ogi et al. 2002; Avkin et al. 2004). POLK can also bypass other DNA lesions including 8oxo-dG caused by oxidative stress in association with Werner syndrome helicase (WRN) protein (Haracska et al. 2002; Maddukuri et al. 2014) and through strand break repair mechanism (Zhang et al. 2013). *Polk*$^{-/-}$ mice showed survival defects, spontaneous mutations, and sensitivity to BPDE (Stancel et al. 2009; Singer et al. 2013). Evidence supports that POLK can function in non-S phase cells through a NER-dependent mechanism to protect from UV-induced cytotoxic lesions (Ogi and Lehmann 2006; Sertic et al. 2018). *Polk*$^{-/-}$ mouse embryo fibroblasts were sensitive to hydrogen peroxide and showed defects in both SSB and DSB repair, suggesting that Polk may have an important role in the oxidative stress-induced DNA repair process (Zhang et al. 2013). Although POLK is associated with multiple DNA repair mechanisms, it remains unknown if normative age-associated DNA damage will also recruit POLK and how it may function in postmitotic neurons.

Unlike the long-living postmitotic neurons that endure DNA damage, the non-neuronal cells can go through the cell cycle and are replaceable. Due to the non-replicative status of differentiated neurons in mature circuits, it is critical to understand the different repair strategies and mechanisms that postmitotic neurons employ to maintain their genomic integrity, which will help design therapies for human longevity and the prevention of neurodegeneration. Here we characterize the expression of POLK in the brain, its subcellular localization, how it is altered with chronological age, cell type-specific variability, and the microglial engagement with neurons, and neuronal activity in wild-type mouse brains undergoing healthy aging under unstressed conditions.

Results:

A progressive age-associated shift in subcellular localization of POLK

POLK has been studied mostly in proliferating cells; however, its levels are found to be highest in the G0 phase of the cell cycle and upregulated upon exposure to exogeneous agent cisplatin in dorsal root neurons (Zhuo et al. 2018). Hence, we explored whether POLK is expressed in the brain, where both replicating and non-replicating cells make it a unique tissue environment. Since neurons endure an onslaught of a lifetime of DNA damage due to activity, genotoxic agents, and physiological age, we investigated if the levels of endogenous POLK in the mice brain also vary as a function of age. In addition, since POLK showed subcellular relocalization in cancer cells undergoing stress (Temprine et al. 2020; Paul et al. 2023), we further explored whether POLK in the brain shows similar changes during normative aging in C57BL/6J (RRID:IMSR_JAX:000664) wild-type mice.

We first validated using mouse primary cortical neurons and other murine cells a published POLK antibody (sc-166667) raised against human POLK protein targeting the epitope 131-310 amino acids, which has complete sequence homology between mouse and human POLK (Figure S1A). Knockdown of POLK in mouse primary cortical neurons (Figure S1B) showed reduction in POLK levels using immunofluorescence (IF) (Figure 1A1), and western blot (WB) (Figure 1A2, S1E); similar reduction of two POLK bands (~99 and 120kDa) were observed in other efficiently transfectable murine cells like Neuro-2A (Figure S1C) and 4T1(Figure S1D). We used another anti-POLK (A12052) that showed similar POLK staining pattern as sc-166667 in mouse brain by immunofluorescence (Figure S1G). From here on onwards for all assays we used anti-POLK antibody SC-166667. We observed a decrease in nuclear POLK bands by WB in mouse cortex unsorted cell nuclear lysate between 7 months and 22 months; however we did not see any changes in the cytoplasmic POLK (Figure 1B, S1F). This prompted a longitudinal unbiased survey of POLK expression across multiple cortical areas at the subcellular level using IF to visualize the

spatial-temporal changes of POLK with age in a healthy wild-type mouse brain; young 1 month, middle age 10 months, and early-old age 18 months mice (Figure 1C).

To visualize the changes in the subcellular level we developed an automated image analysis pipeline using CellProfiler (Stirling et al. 2021) that segments the nucleus and cytoplasm using the fluorescent Nissl signal that primarily stains cell bodies in brain sections (Paul et al. 2008). POLK is detected as small “speckles” inside the nucleus at a young age (1-2 months) and larger “granules” can be seen in the cytoplasm at progressively older time points (>9 months) (Figure 1D). In young brains, both the normalized counts of nuclear POLK speckles and their size are consistent across the cingulate cortex (Cg1), motor cortex (M1 and M2), and somatosensory cortex (S1). A comparison of the nuclear POLK speckle counts and size using ANCOVA shows a significant age-associated decline with medium to large effect sizes across the four brain areas surveyed (Figure 1E-G, Tables 1-2) in agreement with the immunoblot assay. On the other hand, in the cytoplasm, there is a significant age-associated accumulation of POLK in the form of increasingly larger-sized granules with decreasing total counts (Figure 1E, F, H, Tables 3-4). Since cytoplasmic accumulation is non-homogenous in the form of granules, suggesting cytoplasmic POLK accumulation potentially in cytoplasmic organelles or membrane-less biomolecular aggregates. Our cytoplasmic fractionation procedure did not fully extract proteins from such organelles or aggregates, that possibly explains the discrepancy between cytoplasmic POLK observed by biochemical and cell biological assays.

To check if the age-associated decline in nuclear POLK is a more generalized phenomenon in Y-family TLS polymerases we tested the qualitative expression of REV1 and POL iota (POLI) in the mice brain. REV1 protein shows similar expression patterns as clusters of speckles inside the nucleus, a similar qualitative decline in nuclear expression, and an increase in cytoplasmic granules in M1 and S1 brain areas at 1, 10, and 18 months. Comparatively, POLI nuclear expression showed overall lower levels, with decreased age-associated alterations in nuclear

expression, however still showed age-associated cytoplasmic accumulation (Figure S1H). Antibody against Pol eta (POLH) showed a very weak signal or failed.

Nuclear POLK co-localizes with DNA damage response and repair proteins

Various pathways in the DNA damage response have evolved to detect and repair different types of lesions that threaten the genome. Among these, ROS pose a significant threat to the neurons (Attwell and Laughlin 2001), creating ROS-induced DNA modifications 8oxo-dG (Lindahl and Barnes 2000; Madabhushi et al. 2014; Tubbs and Nussenzweig 2017). Repair of 8oxo-dG lesions primarily occurs through BER, where a glycosylase enzyme identifies and removes the damaged base, followed by cleavage of the DNA backbone by apurinic/apyrimidinic endonuclease 1 (APE1), resulting in a single-strand break (SSB). This intermediate can then be processed by polymerase beta (POLb) which fills in the gap with the correct nucleotide, and the nick is sealed by ligase III (LIG3). Along with single-strand breaks (SSBs), double-strand breaks (DSBs) are more harmful due to their potential for toxicity. Despite this toxicity, DSBs also play crucial roles in cellular physiology. For instance, neurons require DSBs to facilitate the expression of immediate early genes (Suberbielle et al. 2013; Madabhushi et al. 2015; Alt and Schwer 2018), particularly through transcriptional activity in postmitotic neurons. Additionally, SSBs may also lead to DSBs (Cannan and Pederson 2016). DSB repair in postmitotic cells is predominantly managed by the non-homologous end joining (NHEJ) pathway. In canonical NHEJ, DSBs are initially recognized and bound at their ends by KU70/80 and DNA-dependent protein kinase (PRKDC). Subsequently, they are directly reconnected through ligation mediated by Ligase IV (LIG4), X-Ray Repair Cross Complementing 4 (XRCC4), and XRCC4-like factor (XLF). At DSB sites, the protein kinase ATM phosphorylates numerous downstream substrates such as histone variant H2A.X, that form gH2AX foci, which are docking sites for DNA repair proteins like p53-binding protein 1 (53BP1) that promote NHEJ mediated DSB repair (Mirman and Lange 2020, Panier and Boulton 2014).

There are hints that TLS polymerases play a role in multiple repair pathways in dividing cells, for example, POLK inserts the correct base opposite the 8oxo-dG lesion and extends from dC:8oxo-dG base pairs supporting potential role in BER (Maddukuri et al. 2014). We previously identified DNA repair pathway proteins by performing iPoKD -MS (isolation of proteins on Pol kappa synthesized DNA followed by mass spectrometry), where proteins were captured and bound to the nascent DNA synthesized by Polk in human cell lines (Paul et al. 2023). Hence, we tested whether neuronal nuclear POLK is associated with BER and NHEJ pathway proteins identified in our iPoKD-MS data sets. We tested 5 NHEJ pathway markers and 4 BER pathway markers at middle age (9-12 months), in the wild-type mouse brain cortex and analyzed the colocalization of these proteins and the markers at the nuclear POLK sites (Figure 2A). Images from the mouse cortex with at least 3 biological replicates per age group were parsed into excitatory pyramidal neurons (PN) and inhibitory interneurons (IN). Nissl+, NeuN+, Gad67+ cells were labeled as IN class and Nissl+, NeuN+, Gad67- as PN class neurons. Each IN and PN class cell bodies were subcellularly segmented into nucleus and cytoplasm and individual nuclear POLK speckles were identified. NHEJ and BER marker intensities were then measured within each nuclear POLK speckles (Figure 2B).

To quantify the association between the DNA damage marker intensities (gH2AX, 53BP1 and 8-oxodG) and POLK levels across age groups and cell types, we first computed Pearson correlation coefficients (r) at the single-cell level. However, because thousands of cells originate from biological replicates, we modeled the relationship using generalized estimating equations (GEE), which estimate population-level effects while explicitly accounting for intra-cluster dependence. GEE assumes a marginal (population-average) linear relationship between the variables and uses a working correlation structure to capture the fact that all cells from the same replicate share similar covariance. For each age-group × cell-type panel, the p value reported reflects a

hypothesis test of the slope relating POLK intensity to the nuclear markers tested within the GEE framework, that is, whether the population-level association are significantly different after accounting for replicate-level clustering. These p values were subsequently Bonferroni-adjusted across panels to control the family-wise error rate. Collectively, this approach provides a conservative estimate of statistical significance and yields inference that is valid at the population level and should be interpreted as population-average relationships across biological replicates, capturing broad trends in how marker intensities covary with POLK across different ages and cell types.

In middle age, for both IN and PN classes, we observed that POLK intensity positively correlated with DSB marker gH2AX (Figure 2C1-2), NHEJ markers 53BP1 (Figure 2D1-2) and PRKDC (Figure 2F1), and ROS-mediated damage marker 8oxo-dG (Figure 2E1-2). Interestingly, BER pathway marker APE1 and to a lesser degree LIG3 were only present in POLK speckles in INs but not in PNs (Figure 2F2-3). In the NHEJ pathway only PRKDC showed high colocalization with nuclear POLK in both IN and PN, but other NHEJ proteins like KU70 and XRCC4, did not colocalize and their intensities were not correlated with POLK levels (FigureS2).

Since both gH2AX and 8oxo-dG were positively associated with the nuclear POLK speckles we wanted to examine if their colocalization and intensity correlation with POLK levels varies with progressive age. So, we further tested early-old (18 months) and late-old (24-27 months) time points. This showed that the temporal profile of gH2AX and 8oxo-dG association with POLK are distinct. Broadly, peak colocalization of gH2AX in POLK speckles was at the early-old time point (Figure 2C3), whereas the presence of 8oxo-dG in POLK speckles declines in early-old age but strikingly increases in the late-old age group (Figure 2E3). The temporal profile of gH2AX intensities in POLK speckles and gH2AX-POLK correlation was mirrored by 53BP1, which is well-known to promote DSB repair through NHEJ pathway, suggesting higher levels of DSBs at early-

old age and spatio-temporal association of POLK. To further inspect if there is differential DNA damage between IN and PN, for each age group, we modeled the mean difference in marker intensities for gH2AX, 53BP1, 8oxo between IN and PN using the same GEE approach. The primary p-values test whether the cluster-adjusted IN versus PN means are significantly different. Across age groups, p-values were corrected using the Benjamini–Hochberg method to control the false discovery rate. Though both INs and PNs showed similar profiles, nuclear POLK speckles had consistently higher levels of gH2AX intensities in INs compared to PNs with the large effect size for 53BP1, throughout all three age groups studied (Figure 2D3), suggesting that nuclear POLK plays a role at DSB sites in INs more compared to PNs. In contrast, there was no difference to ROS induced 8oxo-dG intensities between IN and PNs, as well as decreased 8oxo-dG intensities in middle age (Figure 2E3). We observed POLK association with BER proteins in middle age and reduction in ROS-induced DNA damage, suggesting that POLK plays a role in BER pathway during middle age mostly in INs compared to PNs, and perhaps this capacity of POLK is lost with aging.

Interestingly, we also observed with an increase in age, an elevated neuronal cytoplasmic gH2AX accumulation in the form of granules that colocalized with cytoplasmic POLK. During normal and premature aging syndromes, accumulation of gH2AX-enriched cytoplasmic DNA as cytoplasmic chromatin fragments (CCF) were reported that correlate with inflammatory gene expression and activation of cGAS-STING pathways (Miller, Dasgupta, et al. 2021; Lan et al. 2019; Miller, Victorelli, et al. 2021). In senescent cells, CCFs bud off the nucleus and are processed via lysosomes/autophagy-mediated proteolytic processing (Ivanov et al. 2013), which often accumulates due to lysosomal defects that impairs proteolytic clearance (Carmona-Gutierrez et al. 2016). Our observation of cytoplasmic POLK granules with gH2AX hints towards cytoplasmic sequestration potentially impairing its DNA repair activity and accumulation in lysosomes.

POLK in the cytoplasm is associated with stress granules and lysosomes in old brains

During the process of aging, dysregulated protein homeostasis can occur through widespread intracellular protein aggregates (Taylor and Dillin 2011). A decline in the protein quality control system has been shown to impact the assembly and dynamic maintenance of stress granules (SGs) leading to increased cellular aggregation. SG are nonmembrane assemblies of untranslated mRNAs, RNA-binding proteins, protein translation factors and many non-RNA-binding proteins (Cao et al. 2020; Guzikowski et al. 2019), which can be induced by oxidative stress and other stressors (Federico et al. 2012; Gandhi and Abramov 2012; Patten et al. 2010). Since we observed with increasing age elevated DNA damage markers (Figure 2), and POLK increasingly accumulating in the cytoplasm as "granules" (Figure 1), we hypothesized that cytoplasmic POLK may be present with SG. Ras-GTPase-activating protein (GAP)-binding protein 1 (G3BP1) is a key player in SG assembly often referred to as SG nucleator (Sidibé et al. 2021; Aulas et al. 2015; Sahoo et al. 2018), hence we tested if cytoplasmic POLK granules colocalize with G3BP1. In young (1-month) brains, there was a minimal expression G3BP1, however by the early-old stage (18 months) cytoplasmic POLK is almost entirely colocalized with both G3BP1 (Figure 3B, S3A).

A decline in organelle homeostasis including the endosome-lysosome leading to compromised proteolytic capability is well established in aging neurons (Cheng et al. 2018; Nixon 2020). So, we tested colocalization of cytoplasmic POLK granules with established endo/lysosomal marker proteins. We observed partial colocalization with EEA1, an early endosomal marker (Figure 3C), suggesting cytoplasmic POLK in highly dynamic early endosomes that undergo continual fusion and fission with lysosomes to sort cargo (Christoforidis et al. 1999; Sweet 1999). Lysosomes act as terminal degradative hubs for autophagic and endocytic substrates, supporting neuronal homeostasis necessary for growth, survival, and synaptic remodeling. Lysosomes exist as a continuum of heterogeneous intermediate organelles differing in morphology, membrane composition, hydrolase content, luminal pH, and function (Cai et al.

2010; Farías et al. 2017; Padamsey et al. 2017; Klionsky and Emr 2000; Levine and Klionsky 2004; Maday et al. 2012; Maday and Holzbaur 2014; Nixon 2013; Saftig and Klumperman 2009). In neurons, lysosome-associated membrane proteins (LAMP1)-labeled organelles are heterogeneous, comprising intermediates of endocytic, autophagic pathways and in lysosomal biogenesis. We observed high colocalization of cytoplasmic POLK with LAMP1 in 18-month-old mice neurons (Figure 3B). However, not all LAMP1-positive compartments are degradative due to limited (or undetectable) hydrolase content (Hollenbeck 1993; Lee et al. 2011; Maday et al. 2012; Maday and Holzbaur 2014; Cheng et al. 2015; Gowrishankar et al. 2015; Goo et al. 2017; Cheng et al. 2018c; 2018b). A hallmark of degradative lysosomes is the presence of active hydrolases, such as cathepsins B and D and the glucocerebrosidase GCase. In our imaging, POLK partially colocalized with Cathepsin B (Figure 3D), colocalized robustly with Cathepsin D (Figure 3E), an aspartyl protease residing in the lumen of mature (late endosome) lysosomes often autolysosomes. However, there was minimal colocalization with GBA1/GCase (Figure 3F), a sphingolipid hydrolase that is also imported into mitochondria to support complex-I integrity (Grabowski et al. 1990; Baden et al. 2023; Cheng et al. 2018b). We however did not test any mitochondrial markers. Overall, the data support a model in which cytoplasmic POLK resides highly in endocytic/degradative compartments (CTSD-rich) and associates with SGs in aging neurons.

Differentially altered POLK subcellular expression amongst excitatory, inhibitory, and non-neuronal cells in the cortex.

To further test if the subcellular shift in POLK impacts all cells uniformly, we performed immunostaining of young (1 month) and old (19-24 months) brains to segregate excitatory pyramidal neurons (PN), inhibitory interneurons (IN), and non-neuronal (NN) cells in the mouse cortex. Brain sections were co-immunostained with i) anti-NeuN to detect pan-neuronal protein

RBFOX3, ii) anti-GAD67 to detect GABAergic neurons, iii) fluorescent Nissl to label all cells, and iv) anti-POLK to measure subcellular POLK levels. Our original image quantitation pipeline was modified to register cells positive for GAD67, NeuN, and Nissl as GABAergic interneurons (IN), NeuN and Nissl positives as glutamatergic excitatory pyramidal neurons (PN), and Nissl positives only as non-neuronal (NN) cells (Figure 4A). The INs and PNs were further segmented into their nuclear and cytoplasmic compartments whereas NN subcellular segmentation was not implemented as their nucleus occupies most of the cellular morphology (García-Cabezas et al. 2016) (Figure 4B). Hence in NN, the POLK signal was considered to primarily represent the nuclear compartment. We restricted our survey to the GABAergic inhibitory and glutamatergic excitatory neurons in cortical areas M1 and S1, which have extremely low (<0.01%) cholinergic and almost no dopaminergic, serotonergic, glycinergic, and histaminergic neuronal cell bodies (Zhang et al. 2023). Strikingly, at all ages across the cortical areas observed, the nuclear POLK signal was consistently highest in the cell group identified as INs, followed by PNs and NNs with large effect sizes (Figure 4C, Table 5).

Microglia associated with IN and PN have significantly higher levels of cytoplasmic POLK

Synapses and cell bodies are removed by brain microglia and activated microglia have been associated with various neurological disorders. To test if neurons with higher cytoplasmic POLK granules are vulnerable to microglia engagement, we surveyed by immunostaining with microglia marker protein IBA1 in middle (11 months), early-old (18 months) and late-old (24-27 months) time points. Images were analyzed to register IBA1+ cells as microglia (MG class), GAD67+, NeuN+, and Nissl+ cells as IN class and NeuN+, Gad67-, and Nissl+ cells as PN class (Figure 5A). IN or PNs where MG cells are overlapping or in contact are scored as MG-tied IN or MG-tied PN, and IN and PN cell bodies that are removed by more than one MG cell body length are scored MG-free IN and MG-free PN (Figure 5B). Overall, as expected, MGs are more prevalent at older

ages (Figure 5C). We then compared the cytoplasmic POLK levels between the MG-tied IN and MG-free INs as well as MG-tied and MG-free PNs. Interestingly, early-old MG-tied INs have significantly more cytoplasmic POLK granules intensity and counts compared to MG-free INs and MG-free PNs (Figure 5D, S4). While the mechanism is unknown we speculate loss of MG-tied interneurons in late-old age most likely reflects a survivorship bias, perhaps due to the MG-mediated removal of the INs from the early old stage. Such differences were not noted in nuclear POLK counts between MG-tied and MG-free INs and PNs (Figure S4). Combined with the observations of elevated DNA damage and repair in INs (Figure 2), and higher cytoplasmic POLK levels in MG-tied INs in early old age, suggesting potential increased vulnerability of IN class during aging.

Subcellular localization of POLK is regulated by neuronal activity

Neuronal activity is essential for proper neuronal maturation and circuit plasticity (Yap and Greenberg 2018). High metabolic demands during increased neuronal activity can generate oxidative damage to actively transcribed regions of the genome (Lu et al. 2004). Neuronal activity-induced transcription has been linked with the generation of repeated DSBs at gene regulatory elements, potentially contributing to genome instability (Welch and Tsai 2022; Suberbielle et al. 2013; Madabhushi et al. 2015; Delint-Ramirez et al. 2022; Crowe et al. 2006). Although the coupling of transcription to DNA breaks occurs in all cell types, this process is especially challenging to long-lived neurons that are postmitotic and cannot use replication-dependent DNA repair pathways. With limited regenerative capacity, neurons are unable to replace the damaged cells (Iyama and Wilson 2013). Recently, a neuronal-specific complex NPAS4–NuA4 was identified to be bound to recurrently damaged regulatory elements and recruits additional DNA repair machinery to stimulate the repair, thus coupling neuronal activity to DNA repair (Pollina et al. 2023).

Since we observed a decrease in nuclear POLK and concomitant increase in cytoplasmic POLK with age, as well as nuclear POLK to be associated with BER and NHEJ DNA repair pathways in the mice brain, we tested if POLK subcellular localization can be regulated by neuronal activity and if this regulation is influenced by age. For this, we tested two age groups, young (1-2 month) and early-old (18 month) brains. Following acute slice electrophysiology protocol, mouse brains were extracted, and fresh tissue was sectioned coronally and immersed in oxygenated artificial cerebrospinal fluid (ACSF) and maintained at physiological temperature. Coronal sections from the young or early old brains were split into two hemispheres. One hemisphere was maintained in ACSF only forming the control group, and the other hemisphere was exposed to a bath application of kainic acid (KA), a glutamate receptor agonist that synchronously depolarizes neurons, dissolved in ACSF, which was the treatment group. Each hemisphere either in control ACSF or ACSF+KA were exposed for a duration of 80 mins and 160 mins. After 80min or 160 mins the hemispheres were removed and quickly fixed in 4%PFA to terminate the experiment. The fixed slices were immunolabled for NeuN, fluorescent nissl, c-FOS and POLK to measure changes in c-FOS and POLK protein levels in neurons by IF (Figure 6A). For each age group and exposure (80min and 160min), we ran a non-parametric two-sided Mann–Whitney U test on the dependent variables and computed Cohen's d (KA–CTRL) for effect size.

c-FOS protein is known to be detected by 90 mins sustaining for 2-5 hours upon neuronal activity (Hudson 2018; Kovács 1998), and we observed a robust increase in c-FOS intensity in the nucleus at 160 mins in both young and early-old age groups (Figure 6B). Interestingly, at 160 mins we observed a significant increase in nuclear POLK speckle counts (Figure 6C) and a concomitant decrease in cytoplasmic POLK granules (Figure 6D) in young mice brains. However, such changes in POLK levels were not observed in early-old brains (Figure 6C-D), indicating inducing neuronal activity can elicit a nuclear shift of POLK in young brains which fails in early old brains. Since, we did not distinguish between IN, PN, and NN classes, we cannot exclude the

possibility of even higher differences in activity-induced POLK subcellular localization to the nucleus amongst different cell classes.

Acute brain slice experiments are a powerful assay system for studying synaptic plasticity, circuit organization, and molecular and cellular mechanisms in ex-vivo rodent brains (Nicoll, 2017, PMID: 28061332; Petreanu et al., 2009, PMID: 19151697; Lo et al., 1994, PMID: 7993619; Svoboda & Yasuda, 2006, PMID: 16772166). However, the process of acute brain slices is prolonged and quite different compared to the rapid in-vivo fixation of proteins in an intact brain by vascular PFA perfusion that freezes the cell-molecular milieu. Acute slices impose stressors like transient hypoxia, mechanical trauma of cutting, and initial metabolic shock that can induce c-FOS, CCAAT enhancer binding protein (C/EBP) and brain-derived neurotrophic factor (Taubenfeld et al. 2002) and may cause redox damage (Malkov et al. 2014; D'Agostino et al. 2007; Sasaki et al. 2018), especially in old brains (Ting et al. 2014). Hence directly comparing baseline nuclear POLK in intact brains to ex-vivo slices exposed to prolonged oxygenated ACSF may be inappropriate, as both the young and old slices are in an shared artificial state. This may explain the neuronal POLK baseline levels for young and old being similar in the ex-vivo assay (Figure 6C). Despite these limitations, a timed exposure of acute slices from the same animal to either KA or ACSF provided a uniquely controlled observational opportunity to ask a bigger question, if a Y-family TLS polymerase can at all respond to neuronal activity and within what time scale. Our results provide first direct evidence of POLK shuttling upon neuronal activity within hours, likely to retain it in the nucleus for activity-induced DNA repair process, a capacity that was absent in older brains.

We however do not have an explanation for the surprising temporary initial dip in nuclear POLK puncta seen in both young and old ex-vivo slices only upon KA treatment at 80min with very similar magnitudes, Cohen's d = -0.19 (Figure 6C). Since this activity induced observation is age independent, it may indeed be a hint to an entirely novel biological phenomenon of POLK (and

perhaps TLS polymerases in general) that occurs at a rapid time scale which would not otherwise have been captured in a perfused fixed tissue end-point assay. This will need a detailed investigation using continuous fluorescence imaging of live tissues that is beyond the scope of this current study.

POLK nucleo-cytoplasmic status is a learnable feature of neuronal age

There have been multiple approaches towards estimating biological age using “aging clocks” by sequencing, from tissue and body fluids using epigenetic marks (Grodstein et al. 2020) and multi-omics approaches (Nie et al. 2022). Further genomic instability is increasingly associated with neuronal activity and aging, with Progeroid syndromes are often linked to compromised genomic integrity (Gurkar and Niedernhofer 2015). However, there is a lack of *in situ* methods to determine age from tissues. Hence, we hypothesized that it may be possible to leverage the protein expression of POLK to determine the biological age of brain tissue sections. Specifically, we tested if the naturally occurring shift in the subcellular localization of the endogenous POLK can be a learnable feature that can predict organismal age from brain sections. For this, we used two related non-parametric ensemble-based classifiers Random Forest and Gradient Boosting Machine where 80% of the data was used for training and validation, and then tested on 20% hold-out group. Both learning methods are based on recursive partitioning of the feature space through decision trees. Unlike parametric statistical tests, they do not assume normality, homoscedasticity, or linear relationships between predictors and outcome variables. Instead, these models assume that (a) the input features are relevant and measured without systematic bias, (b) the samples are independent and identically distributed, and (c) the training data sufficiently represent the underlying population to avoid overfitting. Random Forest reduces variance through bagging (bootstrap aggregation) and random feature selection, producing an average prediction across many decorrelated trees. Gradient Boosting, in contrast, sequentially builds trees that correct errors made by prior iterations, minimizing a differentiable loss function

and often achieving higher sensitivity at the cost of greater susceptibility to overfitting. Feature importance was quantified using total increase in node purity (Random Forest) and relative influence (Gradient Boosting), both reflecting the average improvement in model fit attributable to each predictor variable.

We first used the smaller dataset from Figure 1 and parameters like nuclear and cytoplasmic POLK counts, nuclear area, cytoplasmic area, and replicates were tested to examine if organismal age is discernible. Further, using a larger dataset and parameters from Figure 5, where we had observed the association of MG with increased cytoplasmic POLK in IN-class, we tested if finer distinctions between middle, early-old, and late-old age groups are possible. In the smaller dataset (Figure 7 Panels A1–A2, N = 1,232; Train = 788, Validation = 198, Test = 246), both models achieved strong classification performance. The Random Forest model yielded AUROC values of 0.929, 0.775, and 0.856 for 1-, 10-, and 18-month groups, respectively, while the Gradient Boosting model achieved comparable AUROC values of 0.895, 0.775, and 0.838. Across both algorithms, the most influential predictors were cytoplasmic POLK counts per area, cytoplasmic POLK total count, nuclear POLK total count, and nuclear POLK counts per area, followed by morphometric features such as nucleus area and cytoplasm area. (Figure 7A3 and A4). In the larger dataset (Figure 7 Panels A3–A4, N = 28,680; Train = 18,355, Validation = 4,589, Test = 5,736), model performance remained robust. The Random Forest classifier produced AUROC values of 0.804 (10 M), 0.813 (18 M), and 0.871 (24–27 M), while the Gradient Boosting classifier yielded 0.744, 0.768, and 0.846, respectively. In both models, cytoplasmic POLK median intensity, cytoplasmic POLK per area, nuclear POLK median intensity, and cytoplasmic area were the most important features.

Following a similar strategy, using data from young and old groups shown in Figure 4, we observed that in both age groups nuclear POLK speckle counts per unit area alone is the major

driver in distinguishing IN, PN, and NN classes with ROC > 0.8 (Figure 7B1 and B2) suggesting cell classes IN, PN, and NN have an inherent biological requirement in how they utilize TLS polymerase POLK. Together, these analyses indicate that quantitative measures of POLK localization particularly cytoplasmic intensity and spatial distribution can potentially serve as reliable predictors of age-dependent cellular phenotypes. The consistent ranking of variable importance across both modeling approaches supports the robustness of these features in distinguishing neuronal aging stages. Here we recognize that as a terminal assay POLK nucleo-cytoplasmic status is impractical for longitudinal studies. Additional in depth molecular mechanistic studies of POLK sub-cellular shuttling in healthy aging, in neurodegenerative models and upon gerotherapeutic treatments are needed. However, we believe this observed age-association may fill a useful niche as an endogenous in-situ readout of brain tissue age, given the scarcity of such cell-biological markers compared to cell culture systems.

Discussion

TLS polymerases are well-studied as DNA lesion bypass proteins in dividing cells, and recent extensive research identifies their novel roles in a myriad of other cellular processes (Anand et al. 2023; Paniagua and Jacobs 2023). Despite evidence of mRNA expression of the Y-family TLS polymerase *Polk* in IN and PN sub-types (Tasic et al. 2018; Paul et al. 2017), the role of POLK in postmitotic cells has not yet been explored in the central nervous system (CNS). There is only one study of POLK in the peripheral nervous system (PNS), where upon cisplatin treatment *Polk* mRNA was upregulated in dorsal root ganglion (DRG) neurons (Zhuo et al. 2018), and POLK was found essential for efficiently and accurately repairing cisplatin crosslinks (Jha and Ling 2018). In a cell-free system, POLK faithfully bypasses 8oxo-dG (Maddukuri et al. 2014), which is a major DNA lesion in the neurons. Interestingly, Kaplan-Meier survival curves of *Polk*$^{-/-}$ mice showed decreased survival starting at one year compared to wild-type (WT) and heterozygous littermates,

and increased levels of spontaneous mutations (Stancel et al. 2009). Separately, inactivated *Polk* knock-in mice showed a higher frequency of mutations, micronucleated cells, and DNA damage marker gH2AX foci compared to WT mice (Takeiri et al. 2014). In these studies, the effect of *Polk*$^{-/-}$ was not explored in the brain. However, *ApoE−/−;Polk−/−* mice showed enhanced DNA mutagenesis in several organs including the brain probably due to cholesterol-induced adducts (Singer et al. 2013).

Given that DNA damage markers 8oxo-dG and gH2AX are highly correlated with aging, and Polk is associated with multiple DNA repair mechanisms, as well as POLK can function in non-S phase cells (Ogi and Lehmann 2006; Sertic et al. 2018), however, it remained unknown if normative age-associated DNA damage will also recruit POLK and how it may function in postmitotic neurons. This is the first systematic and longitudinal study of Y-family TLS polymerase focusing mostly on the POLK in postmitotic neurons. Here, we found that Y-family TLS polymerases including POLK are highly expressed in several cortical brain areas with characteristic nuclear speckle-like distribution, reminiscent of nuclear foci in dividing cells (Bi et al. 2005; Bergoglio et al. 2002, 1). DNA repair proteins are often found to form dynamic membrane-less biomolecular condensates or “foci” at damaged sites in response to DSBs, the formation of these foci within the proper time are essential for maintenance of genomic integrity, an emerging hypothesis is that the repair condensates are formed via liquid-liquid phase transition (LLPS) (Hyman et al. 2014; Miné-Hattab et al. 2022; Banani et al. 2017)**.** From our human cell line iPoKD-MS data sets (Paul et al. 2023), there are also hints of POLK’s association with proteins of other nuclear biomolecular condensates like paraspeckles, Cajal bodies, PML nuclear bodies, polycomb (PcG) bodies, and the nucleolus. Hence, we speculate that POLK speckles in the neuronal nucleus are also dynamically localized in various biomolecular condensates depending on context that might facilitate DNA repair and other unknown function.

Interestingly, we noted that brain nuclear lysate shows two distinct POLK bands (~120kDa and ~99kDa), with an enrichment of the lower mobility band ~120kDa and absence in the cytoplasmic fractionation. We observed a similar pattern of bands that were present differentially in the chromatin fraction versus the cytoplasmic fraction in human iPSC-derived neurons and multiple other human cancer cell lines that were reduced upon knocking down POLK (unpublished data). Although the 99kDa is the reported POLK band in literature, we do not exactly understand the nature of the higher molecular weight POLK proteins present in the cellular fractionations. We have few hypotheses based on previous literature on other Y-family polymerase-like POLH proteins, as well as our iPoKD-MS data of the POLK interactome in POLK active genomic sites. POLH has been identified to be post-translationally modified (PTM), such as human POLH undergoes O-GlcNAcylation by O-GlcNAc transferase upon DNA damage (Ma et al. 2017), multisite SUMOylation of POLH are essential for the removal of POLH from the DNA damage sites (Guérillon et al. 2020), and Rad18-dependent SUMOylation of POLH is required to target it to the replication fork and prevent under-replicated DNA (Despras et al. 2016). From the existing knowledge it will be important to identify the PTMs of POLK in the neurons and how these modifications assist in POLK subcellular localization and activity. We predict that either the higher molecular weight (potentially modified POLK or another isoform of POLK) is absent in the cytoplasmic fraction or the fractionation procedure is unable to extract the higher molecular weight POLK from particular cytoplasmic organelle like the endo-lysosomes.

Even in the absence of any exogenous chemical or behavioral stressors, in wild-type mice, POLK in neurons localizes to the cytoplasm at least as early as 10-11 months (middle age) and continues to do so with further normative aging. In fact, this nuclear to cytoplasm POLK shuttling could train two ensemble learning models to predict the age of the mouse brain, where cytoplasmic and nuclear POLK counts were the primary featured drivers. Both learning models performed comparatively well, with possible applications as *in situ* immunofluorescence-based indicators of

age-dependent cellular phenotypes. This can be complementary to existing sequencing-based epigenetic clocks (de Lima Camillo et al. 2022; Bell et al. 2019; Prosz et al. 2024; Griffin et al. 2024; Varshavsky et al. 2023; Kerepesi et al. 2021), allowing simultaneous visual read-out of brain tissue age while scoring for various markers for neurodegeneration, cell stress, and age-associated neuropathologies. We believe other TLS proteins may behave similarly, and a combinatorial approach can even increase the age-predictive power. We were able to make even finer distinctions among middle, early, and late-old stages using the cytoplasmic POLK intensity signal. We predict that multiple stressors during the process of neuronal aging is inducing a cytoplasmic shift of POLK, which needs to be further explored to gain mechanistic understanding of neuronal POLK activity.

Upregulation, stabilization, and subcellular shuttling of POLK have been reported earlier in human cancer cells. Upon oncogene inhibition in melanoma, lung and breast cancer cells, POLK expression was increased and localized from cytoplasm to nucleus leading to resistance to the oncogene inhibiting chemotherapy drugs. Treatment with leptomycin B, an exportin-1 inhibitor, increased the accumulation of nuclear POLK, suggesting oncogenic signaling partially regulates nuclear POLK through the export machinery. A similar nuclear localization of POLK also occurred upon inhibition of the kinase mTOR, by induction of ER stress, or by glucose deprivation, as well as rapid export of POLK to the cytoplasm after stress, suggesting dynamic regulation of POLK upon stress. Interestingly, the upregulation and nuclear localization was found not excessively mutagenic (Temprine et al. 2020). In addition, upon carcinogen-induced nucleolar stress, cellular POLK protein stability increased with enrichment of POLK and its activity in the nucleolus, and was identified to play a critical role in recovery from nucleolar stress (Paul et al. 2023). While POLK overexpression in cancer cells is known to drive mutagenesis and chemoresistance, however its increased stability to recover from nucleolar stress and other additional stress

(Temprine et al. 2020; Paul et al. 2023), suggests POLK can multitask based on cellular context, which can be dependent on its catalytic or non-catalytic functions.

Our findings showing progressive loss of nuclear POLK and accumulation in the cytoplasm suggest nuclear POLK plays an important role in protecting neurons from DNA damage at a young age. Decline of nuclear POLK is likely correlated with lack of repair leading to DNA damage accumulation during the normative aging process. Our data further confirms nuclear POLK is associated with neuronal DNA damage as observed by colocalization with DSB (gH2AX) and ROS-mediated DNA damage sites (8oxo-dG), as well as POLK's role in the BER (colocalization with APE1 and LIG3) and NHEJ repair pathways (53BP1 and PRKDC) in the neurons.

An enduring question revolves around the differential vulnerability of neuronal subtypes to DNA damage (Welch and Tsai 2022). Remarkably, we observed POLK's nuclear expression to be cell class-specific, with the highest levels in INs followed by PN and NN. INs and PNs engage in highly demanding cellular functions, both transcriptionally and energetically. While other important and more abundant cell types in the nervous system, such as astrocytes, oligodendrocytes, and microglia, collectively grouped in this study as NN are also vulnerable to DNA damage, but their characteristics differ significantly from neurons. For instance, NNs can be dispensed as they are largely renewable, possess relatively lower energy demands due to slower physiological kinetics, and can re-enter the cell cycle when necessary (Welch and Tsai 2022). These attributes are thought to collectively lessen the dependence of DNA damage repair in glial cells compared to neurons. Hence the observed lowest nuclear expression of POLK in NN at face value can be reconciled with their known biology. On the other hand, a significant fraction of the IN-types like PV basket cells, Chandelier cells, and Martinotti cells across cortical areas have fast-firing kinetics and hence are energetically more demanding (Markram et al. 2004; Tremblay et al. 2016) arguably accumulating more damage and DNA adducts may require the higher nuclear POLK

presence. Here too, the disparity of nuclear POLK was reproducible enough across young and older ages that measuring the nuclear POLK speckle counts per unit area can predict cell class identity using ensemble learning with consistently high AUROCs.

The association between neurons harboring DNA damage, age-associated neuroinflammation, and cell-type vulnerability is an important piece of the puzzle to understand age-associated neurodegeneration under normal physiological conditions (Welch and Tsai 2022). We observed progressive accumulation of cytoplasmic POLK in stress granules and endo/lysosomal compartments with age, possibly due to impaired proteostasis. The colocalization of cytoplasmic gH2AX and POLK granules indicate association with CCF and will be important to understand POLK's role in driving inflammaging.

Interestingly, only microglia-associated INs had significantly higher cytoplasmic POLK suggesting they are more vulnerable to cumulative age-associated changes. One possibility is that the decline in nuclear POLK in INs causes a reduction in DNA repair that may further initiate cGAS-STING immune signaling thereby recruiting microglia (Gulen et al. 2023; Talbot et al. 2023) or higher levels of cytoplasmic POLK coupled with cytoplasmic gH2AX may itself lead to immune activation. Further in-depth molecular mechanistic studies are needed to dissect POLK's role in neuronal cell class-specific genome maintenance and how it intersects with microgliosis during aging.

Another factor contributing to the heightened vulnerability of neurons to genomic damage is their involvement in functional processes like neuronal activity. Such as induced activity of primary neurons with bicuculline or exposure of mice to fear learning was shown to generate DSBs at the promoters of immediate-early genes (Madabhushi et al. 2015; Stott et al. 2021) and even mice experiencing a new environment can induce DSBs in neurons (Suberbielle et al. 2013). These

activity-induced DSBs are thought to aid in the expression of immediate early genes by swiftly resolving topological constraints at their transcription start sites. Here, we showed inducing neuronal activity in brain slices increases nuclear POLK while diminishing cytoplasmic accumulation. While it is an artificial ex-vivo scenario this approach shows that POLK at least in principle is responsive to induced neuronal activity, and we speculate such an increase in nuclear POLK is likely to be involved in activity-induced DNA repair. However, we noticed that this modulatory effect is lost upon aging indicating some yet unknown mechanism at play that remains to be elucidated. Thus, in our study, we provide first-time evidence of Y-family TLS polymerase, POLK's differential expression in CNS cell classes, and its age-associated and activity-induced subcellular changes with implications in microgliosis under non-pathogenic aging conditions.

Figure legends:

Figure 1: POLK subcellular expression changes with increasing age, across multiple cortical regions.

A1) Validation of anti-POLK antibody (sc-166667) by immunofluorescence on mouse primary cortical neuronal cultures treated with Polk siRNA (top row) showing a marked reduction in nuclear POLK levels after 48hrs, compared to scrambled siRNA control (bottom row).

A2) Western blot of mouse primary cortical neuronal culture treated with siPOLK whole cell lysate immunostained with sc-166667 HRP anti-POLK (HRP conjugated) antibody showing ~20% reduction in POLK protein levels compared to siControl.

B) Quantitation of 120kDa and 99kDa POLK bands from western blot using sc-166667 HRP antibody shows a decreasing trend of nuclear POLK levels with progressive age from unsorted cells of the whole mouse cortex. Full blot shown in supplement figure S1E.

C) Experimental design to longitudinally compare POLK cellular localization in mice brains.

D) Immunofluorescence (IF) followed by imaging and analysis using Cell Profiler of mouse brain sections. Visualization of POLK speckles (green) expression using immunohistochemistry in cells labeled by fluorescent-nissl (red) from wild-type mouse brain aged 1 month, and 18 months. Subcellular compartments were segmented and POLK was detected and measured separately inside the nucleus and in the cytoplasm.

E) Representative low (20x) and high magnification (63x) images of Polk expression using IF from Cg1, M1, M2, and S1 cortical regions in ages 1 month (N=3), 10 months (N=2), and 18 months (N=3). POLK (green) and Nissl depicting all cells (purple) (scale bar = 10um).

F) Boxplot showing nuclear and cytoplasmic POLK counts per unit area for each brain region in 1C grouped by age. n denotes the numbers of cells measured per time points under each boxplot.

G) Means plots with 95% confidence intervals showing the nuclear POLK speckle count and size decreasing with increasing age in Cg1, M1, M2, and S1 cortical areas.

H) Means plots with 95% confidence intervals show the cytoplasmic POLK granule count decreasing with a concomitant increase in size with age in Cg1, M1, M2, and S1 cortical areas.

Figure 2. Colocalization and coexpression of POLK with DNA damage marker proteins in POLK nuclear speckles

A) Experimental design to longitudinally compare POLK colocalization with various DNA damage markers in three age group mice brains. Asterix denotes markers that were studied in three age groups, rest were evaluated in middle age only.

B) Schematic of cell class gating logic, registration, sub-cellular segmentation, POLK speckle detection, measurement of POLK counts, and POLK and DNA damage markers/repair protein intensities.

C1) Representative images showing colocalization of gH2AX, and channel separation of POLK, gH2AX, and POLK speckle overlay on POLK and gH2AX. POLK speckles detected inside the nucleus are outlined in yellow. IN class cells are outlined in red, PN class in green.

C2) Scatterplots of gH2AX intensity measured inside POLK nuclear speckle (y-axis) were plotted against POLK intensities (x-axis) shown for INs (red) and PNs (green). The correlation coefficient and p-values are indicated for each.

C3) Dot mean plots with 95% confidence error bars of gH2AX intensities in the y-axis in INs (red) and PNs (green) plotted as a function of age (x-axis).

D1) Representative images showing colocalization of 53BP1, and channel separation of POLK, 53BP1, and POLK speckle overlay on POLK and 53BP1. POLK speckles detected inside the nucleus are outlined in yellow. IN class cells are outlined in red, and PN class in green.

D2) Scatterplots of 53BP1 intensity measured inside POLK nuclear speckle (y-axis) were plotted against POLK intensities (x-axis) shown for INs (red) and PNs (green). The correlation coefficient and p-values are indicated for each.

D3) Dot mean plots with 95% confidence error bars of 53BP1 intensities in the y-axis in INs (red) and PNs (green) plotted as a function of age (x-axis).

E1) Representative images showing colocalization of 8oxo-dG, and channel separation of POLK, 8oxo-dG, and POLK speckle overlay on POLK and 8oxo-dG. POLK speckles detected inside the nucleus are outlined in yellow. IN class cells are outlined in red, and PN class in green.

E2) Scatterplots of 8oxo-dG intensity measured inside POLK nuclear speckle (y-axis) were plotted against POLK intensities (x-axis) shown for INs (red) and PNs (green). The correlation coefficients and p-values are indicated for each.

E3) Dot mean plots with 95% confidence error bars of 8oxo-dG intensities in the y-axis in INs (red) and PNs (green) plotted as a function of age (x-axis).

F1-F3) Left column, merged 63X representative images of IN and PN, with red arrowheads showing line scan area where intensities of POLK and PRKDC (F1), POLK and APE1 (F2), and POLK and LIG3 (F3) were measured. The right columns in F1-F3 shows corresponding IN and PN-derived scatterplots where y-axis shows PRKDC intensities (F1), APE1 (F2), LIG3 (F3), plotted against POLK intensities (x-axis). Separate plots shown for INs (red) and PNs (green). The correlation coefficients and p-values are indicated for each.

Figure 3: Cytoplasmic POLK expression co-localizing with stress granules and lysosomal proteins

A) Schematic of cytoplasmic compartments and condensates and respective markers in parenthesis that were assayed to colocalize with cytoplasmic POLK.

B) Cytoplasmic POLK (green) expression co-localizing with G3BP1 and LAMP1 (red) in fluorescent-nissl stained cells (blue) of mouse brain tissue in 18 months old brain. Line scan in the boxed region shows POLK co-localizing with LAMP1 and G3BP1.

C – F) Cytoplasmic POLK (green), EEA1, CTSB, CTSD and GBA1 (red) in fluorescent-nissl stained cells (blue) of mouse brain tissue in 18 months old brain. Line scan in the boxed region shows level of POLK co-localization with the proteins. Highest colocalization with CTSD, partial with EEA1 and CTSB, and minimal GBA1.

Figure 4: Nuclear POLK is differentially expressed based on cell-type in old brains.

A) Representative image of the detection of inhibitory interneurons (IN), excitatory pyramidal neurons (PN) and non-neuronal (NN) cell bodies using automated image analysis pipeline from a four-channel image of cortical areas from 19 month old brain.

B) Magnified view of the dotted box from subpanel A showing overlay of the nuclear, cytoplasmic segmentation outlines and detection of nuclear POLK speckles and cytoplasmic POLK granules in IN, PN, and NN cells from wild-type mice cortical areas M1 and S1.

C) Boxplots from brain areas show the nuclear POLK count is higher in INs than PNs and NNs across cortical areas in both young and old age groups.

Figure 5: Microglia associated with INs and PNs show significantly higher levels of cytoplasmic POLK expression.

A) Schematic of the experimental design showing age groups, cell class gating logic, scoring spatial interaction, subcellular segmentation, detection, and measurement of POLK in the cytoplasmic compartment.

B) A representative single 20x imaging field shows outlines of detected cell bodies of IN (red), PN (green). Iba1+ microglia (MG) that are attached or wrapped to neurons (MG-tied, filled light pink

and arrows) and microglia that are within one body length of a neuron (blue fill with an asterisk) as well as unassociated microglia (blue fill). Channel separation shown for the four-channel super-resolution confocal image, fluorescent-nissl, NeuN, and Gad67 = IN, fluorescent-nissl, and NeuN = PN, and fluorescent-nissl, and Iba1 = MG.

C) Representative images from M1 and S1 cortical areas shows an overall increase in Iba1-positive cells in early old age compared to young. Yellow arrowheads point to MG-tied neurons.

D) Boxplot showing the difference in cytoplasmic POLK granule median intensity between MG-free and MG-tied INs and PNs across middle, early old, and late old time age groups. T-test p-values and effect sizes are shown for each comparison.

Figure 6: Kainic acid-induced neuronal activity causes POLK subcellular localization in young ex-vivo brain.

A) Schematic of the experimental design showing age groups, ex-vivo treatment of kainic acid, and control groups, followed by, immunostaining, imaging, and the measurement of nuclear and cytoplasmic POLK.

B) Boxplot of c-FOS levels between ACSF control and kainic acid-treated groups at 80min and 160min post-exposure intervals between young and old brains. Due to large number of observations artificially influencing significance, data was randomly subsampled 200 times, each time with 100 cells per group for Wilcoxon rank-sum (Mann–Whitney U) two-sided test. Distribution of subsampled p values and Cohen's are shown in Figure S5A. Median p value and Cohen's d (grey columns in Figure S5A) are reported on the plot.

C) Boxplot of nuclear POLK speckle counts per unit between ACSF control and kainic acid-treated groups at 80min and 160min post-exposure intervals between young and old brains. Wilcoxon

rank-sum (Mann–Whitney U) two-sided test showed a significant increase in nuclear POLK at 160min in the young brains.

D) Boxplot of cytoplasmic POLK granule counts per unit area between ACSF control and kainic acid-treated groups at 80min and 160min post-exposure intervals between young and old brains. Wilcoxon rank-sum (Mann–Whitney U) two-sided test shows there is a significant decrease with small effect size in cytoplasmic granule counts upon kainic acid treatment after 160min in young brains.

E) Boxplot of cytoplasmic POLK granule size measured by area contained, between ACSF control and kainic acid-treated groups at 80min and 160min post-exposure intervals between young and old brains. Due to large number of observations artificially influencing significance, data was randomly subsampled 200 times, each time with 100 cells per group for Wilcoxon rank-sum (Mann–Whitney U) two-sided test. Distribution of subsampled p values and Cohen's are shown in Figure S5B. Median p value and Cohen's d (grey columns in Figure S5B) are reported on the plot.

Figure 7: Subcellular expression of POLK is a learnable feature predictive of organismal age and IN, PN, and NN cell class from mouse brain tissue.

A1-2) Random Forest (A1) and Gradient Boosting (A2) classifier can distinguish between 1-month, 10-month, and 18-month-old age groups upon training on the subcellular nuclear and cytoplasmic distribution of POLK counts using data from figure 1F and 1G. Top bar shows the number of cells used for training, validation, and test samples of the total. Area Under Receiver Operator Curve (AUROC) values show the performance of the classifier for each age group when

tested on the holdout groups. The bar plot shows the relative contribution of the image parameters and image metadata indicating cytoplasmic POLK counts as the major driver.

A3-4) Random Forest (A3) and Gradient Boosting (A4) classifier can distinguish between middle to late-old ages 10-month, 18-month, and 24-27-month age groups upon training on the subcellular nuclear and cytoplasmic distribution of POLK counts, POLK intensities in nuclear speckles and cytoplasmic granules, MG association and other metadata from figure 5. Top bar shows the data split for training, validation and test groups. Major driver of performance is cytoplasmic POLK intensity and counts.

B1-2) Random Forest (B1) and Gradient Boosting (B2) classifier can distinguish between broad IN, PN, and NN cell class with high AUROC values. Nuclear POLK per unit area and nuclear area are the major feature drivers of performance.

Acknowledgments: Work was supported by grant NIH RF1AG072602 / R01AG072602 to AP and Startup Funds from Penn State College of Medicine to A.P.

Author contributions: AP conceived, directed, and planned the work. AP and SP designed the experiments. MA, PP, AP, and SP performed experiments. VV and YS helped MA and PP with experiments with slice preparation and kainic acid experiments. MA, PP, AP, and SP did the analysis, and generated figures. AP wrote the manuscript with help from SP. All authors discussed the results and commented on the manuscript.

Supplemental Figure Legends

Figure S1 associated with Figure 1

S1A) Protein sequence alignment of mouse and human POLK, with the 133-310 amino acid epitope for sc-166667 anti-POLK antibody showing complete homology between species.

S1B-E is validation of sc-166667 POLK antibody using various mouse cells.

S1B) qPCR of Polk transcript shows a 35% reduction upon siRNA against Polk but not scrambled control siRNA. Polh mRNA levels were not affected by siRNA against Polk.

S1C) Western blot immunostained with SC-166667 antiPOLK-HRP antibody of whole cell lysates of two biological replicates of mouse Neuro-2A cells treated with either siPOLK or shPOLK lentivirus, showed a decrease in 99kDa POLK band.

S1D) Western blot immunostained with SC-166667 antiPOLK-HRP antibody of whole cell lysates of three biological replicates of mouse 4T1 cells treated with siPOLK showed a decrease in 99kDa and 120kDa POLK bands.

S1E) Western blot immunostained with SC-166667 antiPOLK-HRP antibody of whole cell lysates of two biological replicates of mouse primary cortical neurons treated with 4 individual shPOLK lentivirus, shows a decrease in 99kDa and 120kDa POLK bands upon treatment with shPOLK#C.

S1F) Full western blot showing all six replicates nucleus and cytoplasmic fractions from 7 and 22 month old whole brain unsorted cells. Quantitation of the 99kDa POLK band did not show a increase, possibly due to inability to extract POLK associated with lysosomal and stress granules (as observed in Fig 3)

S1G) Immunofluorescence staining of wild-type 18-month-old mouse, from brain cortical area S1 shows a similar pattern and distribution of POLK nuclear speckles (arrowheads) and cytoplasmic granules (arrows) using sc-166667 and A12052. The bottom row is a crop of the boxed area in the corresponding top image.

S1H) Representative low (20x) and high magnification (63x) images of REV1 and POLI expression using IF from S1 and M1 cortical regions in ages 1 month, 10 months, and 18 months.

REV1 (green) and Nissl depicting all cells (purple) (scale bar = 10um in 20x image). Arrowheads point nuclear speckles and arrows indicate cytoplasmic granules.

Wild-type mouse brain cortical areas S1 and M1 shows REV1 and POLI punctate nuclear expression resembling speckles and progressive cytoplasmic accumulation with age at 10 and 18 months.

Supplement Figure S2 associated with Figure 2: Scatter plots showing intensity-intensity plots from INs (red) and PNs (green), where y-axis is KU70, XRCC1, and XRCC4, intensity levels plotted against POLK intensities in the x-axis. The correlation coefficients and p-values are indicated for each.

Supplement Figure S3 associated with Figure 3:

S3A) Cytoplasmic POLK (green) expression co-localizing with G3BP1 (blue) in fluorescent-nissl stained cells (purple) of mouse brain tissue from M1 and S1 cortical regions in 18months old brain but not in young 1 month.

S3B) Cytoplasmic POLK (green) expression co-localizing with LAMP1 (blue) in fluorescent-nissl stained cells (purple) of mouse brain tissue from M1 and S1 cortical regions of 18-month brain.

S3C) Additional representative image with channel separation for immunofluorescence staining of wild-type mouse brain cortical areas S1, showing cytoplasmic POLK is colocalized with stress granule marker G3BP1 and endo/lysosomal marker LAMP1. Arrows indicate few representative sites of colocalization in both images.

Supplement Figure S4 associated with Figure 5: Boxplots comparing the nuclear POLK median intensity and cytoplasmic POLK granule count between MG-free and MG-tied INs and PNs across middle, early-old, and late-old time age groups. T-test p-values are shown for each comparison.

Supplement Figure S5 associated with Figure 6:

Boxplots showing the distribution of p-values and Cohen's d values after performing nonparametric test by 200 repeated random subsampling at 100 cells per group from Figure 6B and 6E. Shaded columns shows the values reported in Fig6B and 6E.

Methods

List of antibodies

Reagent	Designation	Source	Identifier	Dilution
Antibody	Mouse anti-PolK (or) DinB Antibody (A-9)	Santa Cruz	Cat#: sc-166667	IF (1:200 & 1:400) WB (1:500)
Antibody	Mouse anti-PolK (Or) DinB Antibody (A-9) HRP	Santa Cruz	sc-166667 HRP	WB (1:500)
Antibody	Mouse anti-PolK	Abclonal	Cat #: A12052	IF (1:8000) WB (1:2000)
Antibody	Mouse anti- REV1	Santa Cruz	Cat #: sc- 393022	IF (1:400)
Antibody	Mouse anti-Poli	Santa Cruz	Cat #: sc-101026	IF (1:400)
Antibody	Guinea Pig anti-NeuN/Fox3	Synaptic Systems	Cat #: 266004	IF (1:500)
Antibody	Mouse anti-Gad67	Millipore	Cat#: MAB5406	IF (1:1000)
Antibody	Rabbit anti-Gamma h2ax	Novus Biologicals	Cat#: NB100-384	IF (1:2000)
Antibody	Rabbit anti-53BP1	Novus Biologicals	Cat #: NB100-304	IF (1:2000)
Antibody	Rabbit anti-8-OHdG	GeneTex	Cat #: GTX35250	IF (1:100)
Antibody	Rabbit anti-DNA-PKcs	ABclonal	Cat #: A7716	IF (1:100)
Antibody	Rabbit anti-XRCC4	ABclonal	Cat #: A18046	IF (1:100)
Antibody	Rabbit anti-DNA Ligase III	ABclonal	Cat #: A13507	IF (1:100)
Antibody	Rabbit anti-Ku70	ABclonal	Cat #: A7330	IF (1:100)
Antibody	Rabbit anti-XRCC1	ABclonal	Cat #: A0442	IF (1:100)
Antibody	Rabbit anti-Ape1	ABclonal	Cat #: A11238	IF (1:100)
Antibody	Rabbit anti-Iba1	Abcam	Cat #: AB178846	IF (1:1000)
Antibody	Mouse anti-G3BP1	DSHB	Cat #: PCRP-G3BP1-2H8	IF (1:18)
Antibody	Rat anti-1D4B (LAMP1)	DSHB	Cat #: AB_528127	IF (1:200)
Antibody	Rabbit anti- cFOS	Synaptic Systems	Cat #: 226008	IF (1:1000)
Antibody	Dylight 405 Goat anti-Guinea Pig	Jackson ImmunoResearch	Cat #: 106475003	IF (1:1000)
Antibody	Alex Fluor 488 Goat anti- Mouse IgG1	Invitrogen	Cat #: A21121	IF (1:1000 & 1:2000)
Antibody	Alex Fluor 488 Donkey anti- Mouse IgG	Invitrogen	Cat #: A32814	IF (1:1000)
Antibody	Alex Fluor 594 Goat anti-Mouse IgG2a	Invitrogen	Cat #: A21135	IF (1:1000)
Antibody	Alex Fluor 594 Goat anti-Rat	Invitrogen	Cat #: A48264	IF (1:1000)
Antibody	Alex Fluor 647 Goat anti-Rabbit	Invitrogen	Cat #: A32733	IF (1:1000)

NeuroTrace 435/455 blue-fluorescent Nissl stain	Nucleic Acids	Invitrogen	Cat #: N21479	IF (1:300)
NeuroTrace 640/660 deep red-fluorescent Nissl stain	Nucleic Acids	Invitrogen	Cat #: N21483	IF (1:300)
Antibody	Alpha Tubulin	Proteintech	Cat#: HRP-66031	WB (1:10,000)
Antibody	Beta Actin	Proteintech	Cat#: HRP-60008	WB (1:10,000)
Antibody	GAPDH	Santa Cruz	Cat #: sc-365062	WB (1:2000)
Antibody	Histone-H3	Santa Cruz	Cat #: sc-517576	WB (1:1000)
Antibody	MAP2	Abcam	Cat#: ab5392	IF (1:10,000)
Antibody	Cathepsin B	ProteinTech	Cat #:12216-1-AP	IF (1:500)
Antibody	Cathepsin D	Proteintech	Cat #: 21327-1-AP	IF (1:500)
Antibody	Glococerebrosidase (GBA)	Sigma-Aldrich	Cat #: G4171	IF (1:500)
Antibody	EEA1	ProteinTech	Cat #: 28347-1-AP	IF (1:500)
Antibody	HRP-conjugated Goat Anti-Mouse IgG(H+L)	ProteinTech	Cat #: SA00001-1	WB (1:10000)

Animals

Animal use approved and overseen by Penn State College of Medicine Institutional Animal Care and Committee and the Penn State College of Medicine Comparative Medicine. The following mouse lines were used: wild-type C57/BL6 (Jackson Laboratory, Stock#000664), *Gad2*$^{tm2(cre)Zjh}$/J (Jackson Laboratory, Stock#010802), and B6.Cg-*Gt(ROSA)26Sor*$^{tm14(CAG\text{-}tdTomato}$ (Jackson Laboratory, Stock #007914). Mice strains *Gad2*$^{tm2(cre)Zjh}$/J and B6.Cg-*Gt(ROSA)26Sor*$^{tm14(CAG\text{-}tdTomato}$ were bred together to generate Gad2; Ai14 for labeling and distinguishing interneurons for experiments under figure 4. Mice were housed in a temperature and humidity-controlled environment in a barrier facility. Mice were kept under a standard 12 h light–dark cycle, with food and water provided ad libitum. For experiments, animals were used at 1-3 months, 9-12 months, 18-19 months, and 24–27 months of age.

Primary Neuronal Culture and siRNA Transfection

Mouse cortical neuronal cells (Thermo Scientific, Cat No. A15585) were obtained from Thermo Scientific and prepared according to the manufacturer's protocol with minor modifications. Briefly, the frozen cells were rapidly thawed and resuspended in complete Neurobasal™ Medium (Cat No. 21103049, Gibco™) supplemented with B-27™ Supplement (Cat No. 17504044, Gibco™) and GlutaMAX™ Supplement (Cat No. 35050061, Gibco™). The cells were counted and seeded

at a density of 100,000–500,000 cells/cm² on pre-coated 24-well plates (coated overnight with poly-D-lysine; Sigma-Aldrich, Cat No. P6407) or at a density of 40,000–200,000 cells/cm² on CC2 Glass 0.7 cm² 8-well chamber slides (Nunc™ Lab-Tek™ II CC2™ Chamber Slide System, Thermo Scientific, Cat No. 154941). The plates and chamber slides were incubated in a 5% CO2 incubator at 37°C. After 24 hours, the medium in each well was removed and replaced with fresh medium. The cells were fed every third day by aspirating half of the medium and replacing it with fresh medium.

At day *in vitro* 10 (DIV10), transfection of primary neuronal cultures with siRNA was performed according to the manufacturer's protocol (Horizon Dharmacon). Briefly, 1 µM of Accell siRNA was mixed with Accell siRNA Delivery Media (Cat No. B-005000; Horizon Discovery) and added to the neurons in complete Neurobasal™ Medium (50/50 v/v). The following siRNAs were used: Accell Mouse Polk siRNA (Cat No. A-048146-13-0050, Dharmacon), Accell Red Non-targeting siRNA (Cat No. D-001960-01-05, Dharmacon), or Accell Non-targeting siRNA pool (Cat No. D-001910-10-05, Dharmacon). A secondary method of transfection was performed using Lipofectamine RNAiMAX reagent (Thermo Fisher) and OptiMEM (Gibco) following the manufacturer's instructions. The siRNAs used were DinB siRNA (m) (sc-60538) and Control siRNA-A (Cat No. sc-37007). Cells were incubated with the siRNA complex in Opti-MEM for 6 hours, followed by replacement with complete Neurobasal™ medium.

Immunocytochemistry

At 24, 48, and 72 hours after transfection, cortical primary neuronal cells were washed with DPBS+ (DPBS containing Ca^{2+} and Mg^{2+}) and fixed with 4% paraformaldehyde (PFA, Electron Microscopy Sciences, Cat No. 19208) for 20 minutes at room temperature. The cells were then washed with DPBS+ three times. Permeabilization was achieved using 0.3% Triton™ X-100 (Thermo Scientific, Cat No. A16046 (diluted in DPBS+) for 5 minutes at room temperature, followed by incubation in blocking solution (DPBS+ containing 5% goat serum and 0.3% Triton™ X-100) for 1 hour. After washing, the cells were incubated with the respective primary antibodies (Table 1) overnight. The next day, cells were incubated with appropriate secondary antibodies (Table 1) for 1 hour. Following additional washes, the chambers were separated from the glass slides, and cells were stained with Hoechst Nucleic Acid Stains (Cat No. H3570, ThermoFisher Scientific). Coverslips were applied using mounting medium, and slides were stored at 4°C. Images were captured using a confocal microscope (LSM) and analyzed using NIH ImageJ software. All experiments were repeated at least three times, with details provided in the figure legends.

Immunofluorescence Assay

Mice were anesthetized with 100-200ul of ketamine and underwent transcardiac perfusion using 1x phosphate buffered saline (PBS, 10x diluted to 1x from Corning, Cat No. 46-013-CM) and 4% PFA made in 0.2M PBS. Brain tissues were fixed with 4% PFA at 4°C degrees for 24hours, post-fixation brains were transferred to 1% sodium azide (Scientific inc., Cat No. DSS24080-250) in 1xPBS. Fixed brains were sectioned coronally at 60µm thickness using a vibratome. For staining, free-floating brain slices underwent blocking consisting of 10% goat serum (Jackson ImmunoResearch, Cat No. 005000121), 1x PBS, and 10% Triton X-100 at RT for 2 hours on an orbital shaker. The following blocking slices were washed 3x with PBS at RT for 10 minutes each

time. Slices were incubated with cocktail mix of 1xPBS, 1% Triton X, 5% goat serum, and primary antibody 4°C degrees for 24hours on an orbital shaker. Post-primary incubation, slices were washed 3x with PBS at RT for 10 minutes each time. Slices were incubated with 1xPBS, 1% Triton X, 5% goat serum, and secondary antibody at RT for 2 hours on an orbital shaker. Slices were washed for 10 minutes on orbital shaker at RT. Slices were incubated with 1xPBS and Nissl for 40 minutes at RT, followed by a final wash with 1xPBS for 10 minutes. Slices were mounted on ColorFrost Microscope slides using mounting media (Invitrogen, Cat No. E142757). Immunofluorescence assay in figure 1 used a slightly different procedure. The blocking buffer used 10% donkey serum instead of goat serum.

Cell Culture, Transfection, and Lentiviral Transduction

N2a (CCL-131; ATCC, USA) and 4T1 (CRL-2539; ATCC, USA) cell lines were cultured in DMEM (Dulbecco's Modified Eagle Medium) and RPMI 1640 medium, respectively, both supplemented with 10% FBS, penicillin (100 IU/mL), and streptomycin (100 µg/mL) (Cat No. 30-002-CI, Corning) in a humidified incubator at 37°C with 5% CO2. After 2 days, siRNA transfection was performed following the manufacturer's protocol (Horizon Dharmacon). Briefly, 1 µM of Accell siRNA was mixed with Accell siRNA Delivery Media and added to cells. The following siRNAs were used: Accell Mouse Polk siRNA (Cat No. A-048146-13-0050, Dharmacon) or Accell Non-targeting siRNA pool (Cat No. D-001910-10-05, Dharmacon). An alternative transfection method was performed using Lipofectamine RNAiMAX reagent (Cat No. 13778150, Thermofisher) and OptiMEM (Gibco) following the manufacturer’s instructions. The siRNAs used were DinB siRNA (mouse) (sc-60538) and Accell Mouse Polk siRNA (Cat No. A-048146-13-0050, Dharmacon), along with Control siRNA-A (Cat No. sc-37007). Cells were incubated with the siRNA complex in Opti-MEM for 6 hours, followed by replacement with complete media. In addition, N2a cells were transduced with lentiviral vectors expressing shPolk (Cat No. TL502663V, Origene) or scrambled shRNA (Cat No. TR30021V, Origene) for 8 hours, followed by replacement with complete media. After 72 hours, cells were collected.

Protein Extraction and Western Blot Analysis

Total protein extracts from mouse brain cortex and primary neuronal cell cultures were prepared using the N-PER™ Neuronal Protein Extraction Reagent (Thermo Scientific, Cat No. 87792) with Halt™ Protease Inhibitor Cocktail (Thermo Scientific, Cat No. 87786) following the manufacturer’s instructions. Nuclear and cytoplasmic proteins from brain cortex tissues were extracted using the Minute™ Cytosolic and Nuclear Extraction Kit for Frozen/Fresh Tissues (Invent Biotechnologies INC, Cat No. NT-032), also following the manufacturer’s instructions. Total protein extracts from N2A and 4T1 cells were prepared using RIPA buffer (Thermo Scientific, Cat No. 89900) with Halt™ Protease Inhibitor Cocktail. Protein concentration was determined using the Pierce™ BCA Protein Assay Kit (Thermo Scientific, Cat No. 23227). Protein samples were boiled at 95°C with 4x Laemmli sample buffer (Bio-Rad, Cat No. 1610747) for 5 minutes. Samples were separated on 4–20% Mini-PROTEAN® TGX™ Precast Protein Gels (Bio-Rad) and transferred to a 0.45 µm LF PVDF membrane using the Trans-Blot® Turbo™ Transfer System (Bio-Rad, Cat No. 1704274). After blocking with 5% non-fat dry milk in phosphate-buffered saline with 0.1% Tween 20 for 1 hour at room temperature, membranes were incubated overnight at 4°C with primary antibodies: Polk (ABclonal), Polk-HRP (Santa Cruz Biotechnology), Alpha Tubulin, β-actin, GAPDH, and Histone-H3. Blots were further incubated with secondary antibody (HRP-conjugated

anti-mouse IgG, 1:10,000) for 1 hour. Bands were detected using SuperSignal Chemiluminescent Substrate (Thermo Scientific) and scanned using the ChemiDoc Imaging System (Bio-Rad). Quantitative analyses were performed using ImageJ software (NIH). Proteins were normalized to the corresponding loading control.

Confocal Microscopy, Image Analysis, Quantification

Imaging was performed using Zeiss LSM910 with AiryScan2 super-resolution in multiplex mode SR-2Y, using 40X water (NA=1.2) and 63X oil (NA=1.4) objectives. All images were captured at 16-bit depth. For the 40X objective, scaling per pixel is 0.078um x 0.078um with an image size of 4084 x 4084 pixels. The scaling for the 63X objective is 0.035um x 0.035um per pixel with an image size of 2860 x 2860 pixels. The imaging parameters such as laser power, digital gain, digital offset, and scan-speed were kept constants for all samples within each experiment. Images were saved as uncompressed .czi files, and imported into the CellProfiler v4.2.6 software, where cells were registered, subcellularly segmented and POLK nuclear speckles and cytoplasmic granules were detected as individual objects and quantified.

Statistical Analysis

Statistical analysis, Wilcoxon rank-sum, ANVOA, ANCOVA, Random Forest and Boosting Classifier were done using opensource software JASP 0.18.3, R Studio v2023.06.1+524, and GraphPad Prism. Plots were generated using R Studio, Python, JASP, and GraphPad exported and composed in Adobe Illustrator.

***Ex Vivo* kainic acid treatment**

Brains from 1-month and 18-month-old C57BL/6J animals were dissected and immediately placed on ice. Brains were placed on the mount and cut through the midline, separating each hemisphere. 1.5% agar was prepared and used for the mold of the brain. The brains were submerged in the ice-cold, oxygenated sucrose dissecting solution (in mM: 183 sucrose, 20 NaCl, 0.5 KCl, 1 MgCl2, 1.4 NaH2PO4, 25 NaHCO3, and 10 glucose). Coronal hemi-slices of 100µm-thickness for IF experiments were prepared using a Compresstome® VF-310-0Z (Precisionary Instruments, LLC) with a double-edged stainless-steel blade. Both hemi-slices were placed in an oxygenated holding solution with a modified artificial cerebrospinal fluid (ACSF) (in mM: 100 sucrose, 60 NaCl, 2.5 KCl, 1.4 NaH2PO4, 1.1 CaCl2, 3.2 MgCl2, 1.2 MgSO4, 22 NaHCO3, 20 glucose, 1 ascorbic acid) for 14 minutes. After 14 minutes, the hemi-slices for control were transferred to an oxygenated standard ACSF solution (in mM: 124 NaCl, 4.4 KCl, 2CaCl2, 2.95 MgSO4, 1 NaH2PO4, 10 glucose, 26 NaHCO3) at 28–32°C. The treatment group received bath application of 1.0uM kainic acid (KA, Millipore Sigma, Cat No. K0250) dissolved in ACSF. Control and KA treated slices were removed from the bath at 80 minutes, and 160 minutes. For IF experiments, slices were fixed in 4% PFA for 30 minutes followed by storage in 1% sodium azide to proceed with IF protocol.

Figure generation: All representative images from the Zeiss.czi files were exported as TIFFs or JPEGs using Zen, FIJI, and CellProfiler. Graphical plots were exported as PDFs from RStudio, JASP, or GraphPad Prism, and subpanels were assembled into final figures using Adobe Illustrator.

Bibliography

Alt, Frederick W., and Bjoern Schwer. 2018. “DNA Double-Strand Breaks as Drivers of Neural Genomic Change, Function, and Disease.” *DNA Repair* 71 (November): 158–63. https://doi.org/10.1016/j.dnarep.2018.08.019.

Amente, Stefano, Giacomo Di Palo, Giovanni Scala, et al. 2019. “Genome-Wide Mapping of 8-Oxo-7,8-Dihydro-2’-Deoxyguanosine Reveals Accumulation of Oxidatively-Generated Damage at DNA Replication Origins within Transcribed Long Genes of Mammalian Cells.” *Nucleic Acids Research* 47 (1): 221–36. https://doi.org/10.1093/nar/gky1152.

Anand, Jay, Lilly Chiou, Carly Sciandra, et al. 2023. “Roles of Trans-Lesion Synthesis (TLS) DNA Polymerases in Tumorigenesis and Cancer Therapy.” *NAR Cancer* 5 (1): zcad005. https://doi.org/10.1093/narcan/zcad005.

Attwell, D., and S. B. Laughlin. 2001. “An Energy Budget for Signaling in the Grey Matter of the Brain.” *Journal of Cerebral Blood Flow and Metabolism: Official Journal of the International Society of Cerebral Blood Flow and Metabolism* 21 (10): 1133–45. https://doi.org/10.1097/00004647-200110000-00001.

Aulas, Anaïs, Guillaume Caron, Christos G. Gkogkas, et al. 2015. “G3BP1 Promotes Stress-Induced RNA Granule Interactions to Preserve Polyadenylated mRNA.” *Journal of Cell Biology* 209 (1): 73–84. https://doi.org/10.1083/jcb.201408092.

Avkin, Sharon, Moshe Goldsmith, Susana Velasco-Miguel, Nicholas Geacintov, Errol C. Friedberg, and Zvi Livneh. 2004. “Quantitative Analysis of Translesion DNA Synthesis across a Benzo[a]Pyrene-Guanine Adduct in Mammalian Cells: THE ROLE OF DNA POLYMERASE κ *.” *Journal of Biological Chemistry* 279 (51): 53298–305. https://doi.org/10.1074/jbc.M409155200.

Baden, Pascale, Maria Jose Perez, Hariam Raji, et al. 2023. “Glucocerebrosidase Is Imported into Mitochondria and Preserves Complex I Integrity and Energy Metabolism.” *Nature Communications* 14 (1): 1930. https://doi.org/10.1038/s41467-023-37454-4.

Banani, Salman F., Hyun O. Lee, Anthony A. Hyman, and Michael K. Rosen. 2017. “Biomolecular Condensates: Organizers of Cellular Biochemistry.” *Nature Reviews. Molecular Cell Biology* 18 (5): 285–98. https://doi.org/10.1038/nrm.2017.7.

Bell, Christopher G., Robert Lowe, Peter D. Adams, et al. 2019. “DNA Methylation Aging Clocks: Challenges and Recommendations.” *Genome Biology* 20 (1): 249. https://doi.org/10.1186/s13059-019-1824-y.

Bergoglio, Valérie, Clarisse Bavoux, Vincent Verbiest, Jean-Sebastien Hoffmann, and Christophe Cazaux. 2002. “Localisation of Human DNA Polymerase Kappa to Replication Foci.” *Journal of Cell Science* 115 (Pt 23): 4413–18. https://doi.org/10.1242/jcs.00162.

Bi, Xiaohui, Damien M. Slater, Haruo Ohmori, and Cyrus Vaziri. 2005. “DNA Polymerase Kappa Is Specifically Required for Recovery from the Benzo[a]Pyrene-Dihydrodiol Epoxide (BPDE)-Induced S-Phase Checkpoint.” *The Journal of Biological Chemistry* 280 (23): 22343–55. https://doi.org/10.1074/jbc.M501562200.

Cai, Qian, Li Lu, Jin-Hua Tian, Yi-Bing Zhu, Haifa Qiao, and Zu-Hang Sheng. 2010. “Snapin-Regulated Late Endosomal Transport Is Critical for Efficient Autophagy-Lysosomal Function in Neurons.” *Neuron* 68 (1): 73–86. https://doi.org/10.1016/j.neuron.2010.09.022.

Caldecott, Keith W., Michael E. Ward, and André Nussenzweig. 2022. “The Threat of Programmed DNA Damage to Neuronal Genome Integrity and Plasticity.” *Nature Genetics* 54 (2): 2. https://doi.org/10.1038/s41588-021-01001-y.

Cannan, Wendy J., and David S. Pederson. 2016. “Mechanisms and Consequences of Double-Strand DNA Break Formation in Chromatin.” *Journal of Cellular Physiology* 231 (1): 3–14. https://doi.org/10.1002/jcp.25048.

Cao, Xiuling, Xuejiao Jin, and Beidong Liu. 2020. “The Involvement of Stress Granules in Aging and Aging-associated Diseases.” *Aging Cell* 19 (4): e13136. https://doi.org/10.1111/acel.13136.

Carmona-Gutierrez, Didac, Adam L. Hughes, Frank Madeo, and Christoph Ruckenstuhl. 2016. “The Crucial Impact of Lysosomes in Aging and Longevity.” *Ageing Research Reviews* 32 (December): 2–12. https://doi.org/10.1016/j.arr.2016.04.009.

Chatterjee, Nimrat, and Graham C. Walker. 2017. “Mechanisms of DNA Damage, Repair, and Mutagenesis.” *Environmental and Molecular Mutagenesis* 58 (5): 235–63. https://doi.org/10.1002/em.22087.

Cheng, Xiu-Tang, Yu-Xiang Xie, Bing Zhou, Ning Huang, Tamar Farfel-Becker, and Zu-Hang Sheng. 2018a. “Characterization of LAMP1-Labeled Nondegradative Lysosomal and Endocytic Compartments in Neurons.” *The Journal of Cell Biology* 217 (9): 3127–39. https://doi.org/10.1083/jcb.201711083.

Cheng, Xiu-Tang, Yu-Xiang Xie, Bing Zhou, Ning Huang, Tamar Farfel-Becker, and Zu-Hang Sheng. 2018b. “Characterization of LAMP1-Labeled Nondegradative Lysosomal and Endocytic Compartments in Neurons.” *The Journal of Cell Biology* 217 (9): 3127–39. https://doi.org/10.1083/jcb.201711083.

Cheng, Xiu-Tang, Yu-Xiang Xie, Bing Zhou, Ning Huang, Tamar Farfel-Becker, and Zu-Hang Sheng. 2018c. “Revisiting LAMP1 as a Marker for Degradative Autophagy-Lysosomal Organelles in the Nervous System.” *Autophagy* 14 (8): 1472–74. https://doi.org/10.1080/15548627.2018.1482147.

Cheng, Xiu-Tang, Bing Zhou, Mei-Yao Lin, Qian Cai, and Zu-Hang Sheng. 2015. “Axonal Autophagosomes Recruit Dynein for Retrograde Transport through Fusion with Late Endosomes.” *The Journal of Cell Biology* 209 (3): 377–86. https://doi.org/10.1083/jcb.201412046.

Chow, Hei-man, and Karl Herrup. 2015. “Genomic Integrity and the Ageing Brain.” *Nature Reviews. Neuroscience* 16 (11): 672–84. https://doi.org/10.1038/nrn4020.

Christoforidis, S., H. M. McBride, R. D. Burgoyne, and M. Zerial. 1999. “The Rab5 Effector EEA1 Is a Core Component of Endosome Docking.” *Nature* 397 (6720): 621–25. https://doi.org/10.1038/17618.

Crowe, Samantha L., Vilen A. Movsesyan, Timothy J. Jorgensen, and Alexei Kondratyev. 2006. “Rapid Phosphorylation of Histone H2A.X Following Ionotropic Glutamate Receptor Activation.” *The European Journal of Neuroscience* 23 (9): 2351–61. https://doi.org/10.1111/j.1460-9568.2006.04768.x.

D’Agostino, Dominic P., Robert W. Putnam, and Jay B. Dean. 2007. “Superoxide (*O2-) Production in CA1 Neurons of Rat Hippocampal Slices Exposed to Graded Levels of Oxygen.” *Journal of Neurophysiology* 98 (2): 1030–41. https://doi.org/10.1152/jn.01003.2006.

Delint-Ramirez, Ilse, Lahiri Konada, Lance Heady, et al. 2022. “Calcineurin Dephosphorylates Topoisomerase IIβ and Regulates the Formation of Neuronal-Activity-Induced DNA Breaks.” *Molecular Cell* 82 (20): 3794-3809.e8. https://doi.org/10.1016/j.molcel.2022.09.012.

Despras, Emmanuelle, Méghane Sittewelle, Caroline Pouvelle, Noémie Delrieu, Agnès M. Cordonnier, and Patricia L. Kannouche. 2016. “Rad18-Dependent SUMOylation of Human Specialized DNA Polymerase Eta Is Required to Prevent under-Replicated DNA.” *Nature Communications* 7 (November): 13326. https://doi.org/10.1038/ncomms13326.

Ding, Yun, Aaron M. Fleming, and Cynthia J. Burrows. 2017. “Sequencing the Mouse Genome for the Oxidatively Modified Base 8-Oxo-7,8-Dihydroguanine by OG-Seq.” *Journal of the American Chemical Society* 139 (7): 2569–72. https://doi.org/10.1021/jacs.6b12604.

Farías, Ginny G., Carlos M. Guardia, Raffaella De Pace, Dylan J. Britt, and Juan S. Bonifacino. 2017. “BORC/Kinesin-1 Ensemble Drives Polarized Transport of Lysosomes into the Axon.” *Proceedings of the National Academy of Sciences of the United States of America* 114 (14): E2955–64. https://doi.org/10.1073/pnas.1616363114.

Federico, Antonio, Elena Cardaioli, Paola Da Pozzo, Patrizia Formichi, Gian Nicola Gallus, and Elena Radi. 2012. “Mitochondria, Oxidative Stress and Neurodegeneration.” *Journal of the Neurological Sciences* 322 (1–2): 254–62. https://doi.org/10.1016/j.jns.2012.05.030.

Gandhi, Sonia, and Andrey Y. Abramov. 2012. “Mechanism of Oxidative Stress in Neurodegeneration.” *Oxidative Medicine and Cellular Longevity* 2012: 428010. https://doi.org/10.1155/2012/428010.

Gao, Yanzhe, Elizabeth Mutter-Rottmayer, Anastasia Zlatanou, Cyrus Vaziri, and Yang Yang. 2017. “Mechanisms of Post-Replication DNA Repair.” *Genes* 8 (2): 2. https://doi.org/10.3390/genes8020064.

García-Cabezas, Miguel Á., Yohan J. John, Helen Barbas, and Basilis Zikopoulos. 2016. “Distinction of Neurons, Glia and Endothelial Cells in the Cerebral Cortex: An Algorithm Based on Cytological Features.” *Frontiers in Neuroanatomy* 10. https://www.frontiersin.org/articles/10.3389/fnana.2016.00107.

Goo, Marisa S., Laura Sancho, Natalia Slepak, et al. 2017. “Activity-Dependent Trafficking of Lysosomes in Dendrites and Dendritic Spines.” *The Journal of Cell Biology* 216 (8): 2499–513. https://doi.org/10.1083/jcb.201704068.

Gowrishankar, Swetha, Peng Yuan, Yumei Wu, et al. 2015. “Massive Accumulation of Luminal Protease-Deficient Axonal Lysosomes at Alzheimer’s Disease Amyloid Plaques.” *Proceedings of the National Academy of Sciences of the United States of America* 112 (28): E3699-3708. https://doi.org/10.1073/pnas.1510329112.

Grabowski, G. A., S. Gatt, and M. Horowitz. 1990. “Acid Beta-Glucosidase: Enzymology and Molecular Biology of Gaucher Disease.” *Critical Reviews in Biochemistry and Molecular Biology* 25 (6): 385–414. https://doi.org/10.3109/10409239009090616.

Griffin, Patrick T., Alice E. Kane, Alexandre Trapp, et al. 2024. “TIME-Seq Reduces Time and Cost of DNA Methylation Measurement for Epigenetic Clock Construction.” *Nature Aging* 4 (2): 261–74. https://doi.org/10.1038/s43587-023-00555-2.

Grodstein, Francine, Bernardo Lemos, Lei Yu, Artemis Iatrou, Philip L. De Jager, and David A. Bennett. 2020. “Characteristics of Epigenetic Clocks Across Blood and Brain Tissue in Older Women and Men.” *Frontiers in Neuroscience* 14: 555307. https://doi.org/10.3389/fnins.2020.555307.

Guérillon, Claire, Stine Smedegaard, Ivo A. Hendriks, Michael L. Nielsen, and Niels Mailand. 2020. “Multisite SUMOylation Restrains DNA Polymerase η Interactions with DNA Damage Sites.” *The Journal of Biological Chemistry* 295 (25): 8350–62. https://doi.org/10.1074/jbc.RA120.013780.

Gulen, Muhammet F., Natasha Samson, Alexander Keller, et al. 2023. “cGAS–STING Drives Ageing-Related Inflammation and Neurodegeneration.” *Nature* 620 (7973): 374–80. https://doi.org/10.1038/s41586-023-06373-1.

Guo, Caixia, J. Nicole Kosarek-Stancel, Tie-Shan Tang, and Errol C. Friedberg. 2009. “Y-Family DNA Polymerases in Mammalian Cells.” *Cellular and Molecular Life Sciences: CMLS* 66 (14): 2363–81. https://doi.org/10.1007/s00018-009-0024-4.

Gurkar, Aditi U., and Laura J. Niedernhofer. 2015. “Comparison of Mice with Accelerated Aging Caused by Distinct Mechanisms.” *Experimental Gerontology*, Proceedings of the Twelfth International Symposium on the Neurobiology and Neuroendocrinology of Aging, Bregenz, Austria July 27–August 1, 2014, vol. 68 (August): 43–50. https://doi.org/10.1016/j.exger.2015.01.045.

Guzikowski, Anna R., Yang S. Chen, and Brian M. Zid. 2019. “Stress-Induced mRNP Granules: Form and Function of Processing Bodies and Stress Granules.” *Wiley Interdisciplinary Reviews. RNA* 10 (3): e1524. https://doi.org/10.1002/wrna.1524.

Haracska, Lajos, Louise Prakash, and Satya Prakash. 2002. “Role of Human DNA Polymerase Kappa as an Extender in Translesion Synthesis.” *Proceedings of the National Academy of Sciences of the United States of America* 99 (25): 25. https://doi.org/10.1073/pnas.252524999.

Hoeijmakers, Jan H. J. 2009. “DNA Damage, Aging, and Cancer.” *The New England Journal of Medicine* 361 (15): 1475–85. https://doi.org/10.1056/NEJMra0804615.

Hollenbeck, P. J. 1993. “Products of Endocytosis and Autophagy Are Retrieved from Axons by Regulated Retrograde Organelle Transport.” *The Journal of Cell Biology* 121 (2): 305–15. https://doi.org/10.1083/jcb.121.2.305.

Hudson, Andrew E. 2018. “Genetic Reporters of Neuronal Activity: C-Fos and G-CaMP6.” *Methods in Enzymology* 603: 197–220. https://doi.org/10.1016/bs.mie.2018.01.023.

Hyman, Anthony A., Christoph A. Weber, and Frank Jülicher. 2014. “Liquid-Liquid Phase Separation in Biology.” *Annual Review of Cell and Developmental Biology* 30: 39–58. https://doi.org/10.1146/annurev-cellbio-100913-013325.

Ivanov, Andre, Jeff Pawlikowski, Indrani Manoharan, et al. 2013. “Lysosome-Mediated Processing of Chromatin in Senescence.” *The Journal of Cell Biology* 202 (1): 129–43. https://doi.org/10.1083/jcb.201212110.

Iyama, Teruaki, and David M. Wilson. 2013. “DNA Repair Mechanisms in Dividing and Non-Dividing Cells.” *DNA Repair* 12 (8): 620–36. https://doi.org/10.1016/j.dnarep.2013.04.015.

Jałoszyński, Paweł, Eiji Ohashi, Haruo Ohmori, and Susumu Nishimura. 2005. “Error-Prone and Inefficient Replication across 8-Hydroxyguanine (8-Oxoguanine) in Human and Mouse Ras Gene Fragments by DNA Polymerase Kappa.” *Genes to Cells: Devoted to Molecular & Cellular Mechanisms* 10 (6): 6. https://doi.org/10.1111/j.1365-2443.2005.00858.x.

Jha, Vikash, and Hong Ling. 2018. “Structural Basis for Human DNA Polymerase Kappa to Bypass Cisplatin Intrastrand Cross-Link (Pt-GG) Lesion as an Efficient and Accurate Extender.” *Journal of Molecular Biology* 430 (11): 1577–89. https://doi.org/10.1016/j.jmb.2018.04.023.

Kamiya, Hiroyuki, and Masahiro Kurokawa. 2012. “Mutagenic Bypass of 8-Oxo-7,8-Dihydroguanine (8-Hydroxyguanine) by DNA Polymerase κ in Human Cells.” *Chemical Research in Toxicology* 25 (8): 8. https://doi.org/10.1021/tx300259x.

Kanemaru, Yuki, Tetsuya Suzuki, Akira Sassa, et al. 2017. “DNA Polymerase Kappa Protects Human Cells against MMC-Induced Genotoxicity through Error-Free Translesion DNA Synthesis.” *Genes and Environment* 39 (January): 6. https://doi.org/10.1186/s41021-016-0067-3.

Kerepesi, Csaba, Bohan Zhang, Sang-Goo Lee, Alexandre Trapp, and Vadim N. Gladyshev. 2021. “Epigenetic Clocks Reveal a Rejuvenation Event during Embryogenesis Followed by Aging.” *Science Advances* 7 (26): eabg6082. https://doi.org/10.1126/sciadv.abg6082.

Klionsky, D. J., and S. D. Emr. 2000. “Autophagy as a Regulated Pathway of Cellular Degradation.” *Science (New York, N.Y.)* 290 (5497): 1717–21. https://doi.org/10.1126/science.290.5497.1717.

Kovács, K. J. 1998. “C-Fos as a Transcription Factor: A Stressful (Re)View from a Functional Map.” *Neurochemistry International* 33 (4): 287–97. https://doi.org/10.1016/s0197-0186(98)00023-0.

Lan, Yuk Yuen, James M. Heather, Thomas Eisenhaure, et al. 2019. “Extranuclear DNA Accumulates in Aged Cells and Contributes to Senescence and Inflammation.” *Aging Cell* 18 (2): e12901. https://doi.org/10.1111/acel.12901.

Lee, Sooyeon, Yutaka Sato, and Ralph A. Nixon. 2011. “Primary Lysosomal Dysfunction Causes Cargo-Specific Deficits of Axonal Transport Leading to Alzheimer-like Neuritic Dystrophy.” *Autophagy* 7 (12): 1562–63. https://doi.org/10.4161/auto.7.12.17956.

Lehmann, Alan R. 2006. “Translesion Synthesis in Mammalian Cells.” *Experimental Cell Research* 312 (14): 2673–76. https://doi.org/10.1016/j.yexcr.2006.06.010.

Levine, Beth, and Daniel J. Klionsky. 2004. “Development by Self-Digestion: Molecular Mechanisms and Biological Functions of Autophagy.” *Developmental Cell* 6 (4): 463–77. https://doi.org/10.1016/s1534-5807(04)00099-1.

Lima Camillo, Lucas Paulo de, Louis R. Lapierre, and Ritambhara Singh. 2022. “A Pan-Tissue DNA-Methylation Epigenetic Clock Based on Deep Learning.” *Npj Aging* 8 (1): 1–15. https://doi.org/10.1038/s41514-022-00085-y.

Lindahl, T., and D. E. Barnes. 2000. “Repair of Endogenous DNA Damage.” *Cold Spring Harbor Symposia on Quantitative Biology* 65: 127–33. https://doi.org/10.1101/sqb.2000.65.127.

London, Robert E. 2020. “XRCC1 - Strategies for Coordinating and Assembling a Versatile DNA Damage Response.” *DNA Repair* 93 (September): 102917. https://doi.org/10.1016/j.dnarep.2020.102917.

Lu, Tao, Ying Pan, Shyan-Yuan Kao, et al. 2004. “Gene Regulation and DNA Damage in the Ageing Human Brain.” *Nature* 429 (6994): 883–91. https://doi.org/10.1038/nature02661.

Ma, Xiaolu, Hongmei Liu, Jing Li, et al. 2017. “Polη O-GlcNAcylation Governs Genome Integrity during Translesion DNA Synthesis.” *Nature Communications* 8 (December): 1941. https://doi.org/10.1038/s41467-017-02164-1.

Madabhushi, Ram, Fan Gao, Andreas R. Pfenning, et al. 2015. “Activity-Induced DNA Breaks Govern the Expression of Neuronal Early-Response Genes.” *Cell* 161 (7): 1592–605. https://doi.org/10.1016/j.cell.2015.05.032.

Madabhushi, Ram, Ling Pan, and Li-Huei Tsai. 2014. “DNA Damage and Its Links to Neurodegeneration.” *Neuron* 83 (2): 266–82. https://doi.org/10.1016/j.neuron.2014.06.034.

Maday, Sandra, and Erika L. F. Holzbaur. 2014. “Autophagosome Biogenesis in Primary Neurons Follows an Ordered and Spatially Regulated Pathway.” *Developmental Cell* 30 (1): 71–85. https://doi.org/10.1016/j.devcel.2014.06.001.

Maday, Sandra, Karen E. Wallace, and Erika L. F. Holzbaur. 2012. “Autophagosomes Initiate Distally and Mature during Transport toward the Cell Soma in Primary Neurons.” *The Journal of Cell Biology* 196 (4): 407–17. https://doi.org/10.1083/jcb.201106120.

Maddukuri, Leena, Amit Ketkar, Sarah Eddy, Maroof K. Zafar, and Robert L. Eoff. 2014. “The Werner Syndrome Protein Limits the Error-Prone 8-Oxo-dG Lesion Bypass Activity of Human DNA Polymerase Kappa.” *Nucleic Acids Research* 42 (19): 19. https://doi.org/10.1093/nar/gku913.

Malkov, Anton, Anton I. Ivanov, Irina Popova, et al. 2014. “Reactive Oxygen Species Initiate a Metabolic Collapse in Hippocampal Slices: Potential Trigger of Cortical Spreading Depression.” *Journal of Cerebral Blood Flow and Metabolism: Official Journal of the International Society of Cerebral Blood Flow and Metabolism* 34 (9): 1540–49. https://doi.org/10.1038/jcbfm.2014.121.

Markkanen, Enni. 2017. “Not Breathing Is Not an Option: How to Deal with Oxidative DNA Damage.” *DNA Repair* 59 (November): 82–105. https://doi.org/10.1016/j.dnarep.2017.09.007.

Markram, Henry, Maria Toledo-Rodriguez, Yun Wang, Anirudh Gupta, Gilad Silberberg, and Caizhi Wu. 2004. “Interneurons of the Neocortical Inhibitory System.” *Nature Reviews. Neuroscience* 5 (10): 793–807. https://doi.org/10.1038/nrn1519.

McKinnon, Peter J. 2017. “Genome Integrity and Disease Prevention in the Nervous System.” *Genes & Development* 31 (12): 1180–94. https://doi.org/10.1101/gad.301325.117.

Miller, Karl N., Nirmalya Dasgupta, Tianhui Liu, Peter D. Adams, and Maria Grazia Vizioli. 2021. "Cytoplasmic Chromatin Fragments-from Mechanisms to Therapeutic Potential." *eLife* 10 (January): e63728. https://doi.org/10.7554/eLife.63728.

Miller, Karl N., Stella G. Victorelli, Hanna Salmonowicz, et al. 2021. "Cytoplasmic DNA: Sources, Sensing, and Role in Aging and Disease." *Cell* 184 (22): 5506–26. https://doi.org/10.1016/j.cell.2021.09.034.

Miné-Hattab, Judith, Siyu Liu, and Angela Taddei. 2022. "Repair Foci as Liquid Phase Separation: Evidence and Limitations." *Genes* 13 (10): 1846. https://doi.org/10.3390/genes13101846.

Mirman, Zachary, and Titia de Lange. 2020. "53BP1: A DSB Escort." *Genes & Development* 34 (1–2): 7–23. https://doi.org/10.1101/gad.333237.119.

Nie, Chao, Yan Li, Rui Li, et al. 2022. "Distinct Biological Ages of Organs and Systems Identified from a Multi-Omics Study." *Cell Reports* 38 (10): 110459. https://doi.org/10.1016/j.celrep.2022.110459.

Nixon, Ralph A. 2013. "The Role of Autophagy in Neurodegenerative Disease." *Nature Medicine* 19 (8): 983–97. https://doi.org/10.1038/nm.3232.

Nixon, Ralph A. 2020. "The Aging Lysosome: An Essential Catalyst for Late-Onset Neurodegenerative Diseases." *Biochimica et Biophysica Acta. Proteins and Proteomics* 1868 (9): 140443. https://doi.org/10.1016/j.bbapap.2020.140443.

Ogi, Tomoo, and Alan R. Lehmann. 2006. "The Y-Family DNA Polymerase Kappa (Pol Kappa) Functions in Mammalian Nucleotide-Excision Repair." *Nature Cell Biology* 8 (6): 640–42. https://doi.org/10.1038/ncb1417.

Ogi, Tomoo, Yoichi Shinkai, Kiyoji Tanaka, and Haruo Ohmori. 2002. "Polkappa Protects Mammalian Cells against the Lethal and Mutagenic Effects of Benzo[a]Pyrene." *Proceedings of the National Academy of Sciences of the United States of America* 99 (24): 15548–53. https://doi.org/10.1073/pnas.222377899.

Padamsey, Zahid, Lindsay McGuinness, Scott J. Bardo, et al. 2017. "Activity-Dependent Exocytosis of Lysosomes Regulates the Structural Plasticity of Dendritic Spines." *Neuron* 93 (1): 132–46. https://doi.org/10.1016/j.neuron.2016.11.013.

Paniagua, Inés, and Jacqueline J. L. Jacobs. 2023. "Freedom to Err: The Expanding Cellular Functions of Translesion DNA Polymerases." *Molecular Cell* 83 (20): 3608–21. https://doi.org/10.1016/j.molcel.2023.07.008.

Panier, Stephanie, and Simon J. Boulton. 2014. "Double-Strand Break Repair: 53BP1 Comes into Focus." *Nature Reviews Molecular Cell Biology* 15 (1): 7–18. https://doi.org/10.1038/nrm3719.

Patten, David A., Marc Germain, Melissa A. Kelly, and Ruth S. Slack. 2010. "Reactive Oxygen Species: Stuck in the Middle of Neurodegeneration." *Journal of Alzheimer's Disease: JAD* 20 Suppl 2: S357-367. https://doi.org/10.3233/JAD-2010-100498.

Paul, Anirban, Megan Crow, Ricardo Raudales, Miao He, Jesse Gillis, and Z. Josh Huang. 2017. "Transcriptional Architecture of Synaptic Communication Delineates GABAergic Neuron Identity." *Cell* 171 (3): 522-539.e20. https://doi.org/10.1016/j.cell.2017.08.032.

Paul, Carol Ann, Barbara Beltz, and Joanne Berger-Sweeney. 2008. "The Nissl Stain: A Stain for Cell Bodies in Brain Sections." *Cold Spring Harbor Protocols* 2008 (9): pdb.prot4805. https://doi.org/10.1101/pdb.prot4805.

Paul, Shilpi, Abbey Rebok, Paolo Cifani, et al. 2023. "Translesion DNA Synthesis Polymerase κ Is Essential to a Carcinogen-Induced Nucleolar Stress Response." Preprint, bioRxiv, October 19. https://doi.org/10.1101/2022.10.27.513845.

Pollina, Elizabeth A., Daniel T. Gilliam, Andrew T. Landau, et al. 2023. "A NPAS4–NuA4 Complex Couples Synaptic Activity to DNA Repair." *Nature* 614 (7949): 732–41. https://doi.org/10.1038/s41586-023-05711-7.

Powers, Kyle T., and M. Todd Washington. 2018. “Eukaryotic Translesion Synthesis: Choosing the Right Tool for the Job.” *DNA Repair* 71 (November): 127–34. https://doi.org/10.1016/j.dnarep.2018.08.016.

Prosz, Aurel, Orsolya Pipek, Judit Börcsök, et al. 2024. “Biologically Informed Deep Learning for Explainable Epigenetic Clocks.” *Scientific Reports* 14 (1): 1306. https://doi.org/10.1038/s41598-023-50495-5.

Reid, Dylan A., Patrick J. Reed, Johannes C. M. Schlachetzki, et al. 2021. “Incorporation of a Nucleoside Analog Maps Genome Repair Sites in Postmitotic Human Neurons.” *Science (New York, N.Y.)* 372 (6537): 91–94. https://doi.org/10.1126/science.abb9032.

Saftig, Paul, and Judith Klumperman. 2009. “Lysosome Biogenesis and Lysosomal Membrane Proteins: Trafficking Meets Function.” *Nature Reviews. Molecular Cell Biology* 10 (9): 623–35. https://doi.org/10.1038/nrm2745.

Sahoo, Pabitra K., Seung Joon Lee, Poonam B. Jaiswal, et al. 2018. “Axonal G3BP1 Stress Granule Protein Limits Axonal mRNA Translation and Nerve Regeneration.” *Nature Communications* 9 (1): 3358. https://doi.org/10.1038/s41467-018-05647-x.

Sale, Julian E., Alan R. Lehmann, and Roger Woodgate. 2012. “Y-Family DNA Polymerases and Their Role in Tolerance of Cellular DNA Damage.” *Nature Reviews Molecular Cell Biology* 13 (3): 141–52. https://doi.org/10.1038/nrm3289.

Sasaki, Toru, Takuji Awaji, Kazuyoshi Shimada, and Haruyo Sasaki. 2018. *Increased Levels of Reactive Oxygen Species in Brain Slices after Transient Hypoxia Induced By a Reduced Oxygen Supply*. 8 (2): 684–90. https://doi.org/10.4172/Neuropsychiatry.1000392.

Sertic, Sarah, Antonio Mollica, Ilaria Campus, et al. 2018. “Coordinated Activity of Y Family TLS Polymerases and EXO1 Protects Non-S Phase Cells from UV-Induced Cytotoxic Lesions.” *Molecular Cell* 70 (1): 34-47.e4. https://doi.org/10.1016/j.molcel.2018.02.017.

Sidibé, Hadjara, Alicia Dubinski, and Christine Vande Velde. 2021. “The Multi-Functional RNA-Binding Protein G3BP1 and Its Potential Implication in Neurodegenerative Disease.” *Journal of Neurochemistry* 157 (4): 944–62. https://doi.org/10.1111/jnc.15280.

Singer, William D., Lindsey C. Osimiri, and Errol C. Friedberg. 2013. “Increased Dietary Cholesterol Promotes Enhanced Mutagenesis in DNA Polymerase Kappa-Deficient Mice.” *DNA Repair* 12 (10): 817–23. https://doi.org/10.1016/j.dnarep.2013.07.010.

Stancel, J. Nicole Kosarek, Lisa D. McDaniel, Susana Velasco, James Richardson, Caixia Guo, and Errol C. Friedberg. 2009. “Polk Mutant Mice Have a Spontaneous Mutator Phenotype.” *DNA Repair* 8 (12): 1355–62. https://doi.org/10.1016/j.dnarep.2009.09.003.

Stirling, David R., Madison J. Swain-Bowden, Alice M. Lucas, Anne E. Carpenter, Beth A. Cimini, and Allen Goodman. 2021. “CellProfiler 4: Improvements in Speed, Utility and Usability.” *BMC Bioinformatics* 22 (1): 433. https://doi.org/10.1186/s12859-021-04344-9.

Stott, Ryan T., Oleg Kritsky, and Li-Huei Tsai. 2021. “Profiling DNA Break Sites and Transcriptional Changes in Response to Contextual Fear Learning.” *PLOS ONE* 16 (7): e0249691. https://doi.org/10.1371/journal.pone.0249691.

Suberbielle, Elsa, Pascal E. Sanchez, Alexxai V. Kravitz, et al. 2013. “Physiologic Brain Activity Causes DNA Double-Strand Breaks in Neurons, with Exacerbation by Amyloid-β.” *Nature Neuroscience* 16 (5): 613–21. https://doi.org/10.1038/nn.3356.

Sweet, D. 1999. “The SAC, EEA1, Rab5 and Endosome Fusion.” *Trends in Cell Biology* 9 (4): 149. https://doi.org/10.1016/S0962-8924(99)01543-3.

Takeiri, Akira, Naoko A. Wada, Shigeki Motoyama, et al. 2014. “In Vivo Evidence That DNA Polymerase Kappa Is Responsible for Error-Free Bypass across DNA Cross-Links Induced by Mitomycin C.” *DNA Repair* 24 (December): 113–21. https://doi.org/10.1016/j.dnarep.2014.09.002.

Talbot, Emily J, Lisha Joshi, Peter Thornton, et al. 2023. “cGAS-STING Signalling Regulates Microglial Chemotaxis in Genome Instability.” *Nucleic Acids Research* 52 (3): 1188–206. https://doi.org/10.1093/nar/gkad1184.

Tasic, Bosiljka, Zizhen Yao, Lucas T. Graybuck, et al. 2018. “Shared and Distinct Transcriptomic Cell Types across Neocortical Areas.” *Nature* 563 (7729): 7729. https://doi.org/10.1038/s41586-018-0654-5.

Taubenfeld, Stephen M., Kimberly A. Stevens, Gabriella Pollonini, Jason Ruggiero, and Cristina M. Alberini. 2002. “Profound Molecular Changes Following Hippocampal Slice Preparation: Loss of AMPA Receptor Subunits and Uncoupled mRNA/Protein Expression.” *Journal of Neurochemistry* 81 (6): 1348–60. https://doi.org/10.1046/j.1471-4159.2002.00936.x.

Taylor, Rebecca C., and Andrew Dillin. 2011. “Aging as an Event of Proteostasis Collapse.” *Cold Spring Harbor Perspectives in Biology* 3 (5): a004440. https://doi.org/10.1101/cshperspect.a004440.

Temprine, Kelsey, Nathaniel R. Campbell, Richard Huang, et al. 2020. “Regulation of the Error-Prone DNA Polymerase Polκ by Oncogenic Signaling and Its Contribution to Drug Resistance.” Research Article. *Science Signaling* 13 (629). https://doi.org/10.1126/scisignal.aau1453.

Ting, Jonathan T., Tanya L. Daigle, Qian Chen, and Guoping Feng. 2014. “Acute Brain Slice Methods for Adult and Aging Animals: Application of Targeted Patch Clamp Analysis and Optogenetics.” *Methods in Molecular Biology (Clifton, N.J.)* 1183: 221–42. https://doi.org/10.1007/978-1-4939-1096-0_14.

Tremblay, Robin, Soohyun Lee, and Bernardo Rudy. 2016. “GABAergic Interneurons in the Neocortex: From Cellular Properties to Circuits.” *Neuron* 91 (2): 260–92. https://doi.org/10.1016/j.neuron.2016.06.033.

Tubbs, Anthony, and André Nussenzweig. 2017. “Endogenous DNA Damage as a Source of Genomic Instability in Cancer.” *Cell* 168 (4): 644–56. https://doi.org/10.1016/j.cell.2017.01.002.

Vaisman, Alexandra, and Roger Woodgate. 2017. “Translesion DNA Polymerases in Eukaryotes: What Makes Them Tick?” *Critical Reviews in Biochemistry and Molecular Biology* 52 (3): 274–303. https://doi.org/10.1080/10409238.2017.1291576.

Varshavsky, Miri, Gil Harari, Benjamin Glaser, Yuval Dor, Ruth Shemer, and Tommy Kaplan. 2023. “Accurate Age Prediction from Blood Using a Small Set of DNA Methylation Sites and a Cohort-Based Machine Learning Algorithm.” *Cell Reports Methods* 3 (9): 100567. https://doi.org/10.1016/j.crmeth.2023.100567.

Welch, Gwyneth, and Li-Huei Tsai. 2022. “Mechanisms of DNA Damage-Mediated Neurotoxicity in Neurodegenerative Disease.” *EMBO Reports* 23 (6): e54217. https://doi.org/10.15252/embr.202154217.

Wu, Wei, Sarah E. Hill, William J. Nathan, et al. 2021. “Neuronal Enhancers Are Hotspots for DNA Single-Strand Break Repair.” *Nature* 593 (7859): 7859. https://doi.org/10.1038/s41586-021-03468-5.

Yan, Shan, and Cyrus Vaziri. 2020. “An Introduction for the Special Issue on Environmental Health and Genome Integrity.” *Environmental and Molecular Mutagenesis* 61 (7): 660–63. https://doi.org/10.1002/em.22400.

Yap, Ee-Lynn, and Michael E. Greenberg. 2018. “Activity-Regulated Transcription: Bridging the Gap between Neural Activity and Behavior.” *Neuron* 100 (2): 330–48. https://doi.org/10.1016/j.neuron.2018.10.013.

Zhang, Meng, Xingjie Pan, Won Jung, et al. 2023. “Molecularly Defined and Spatially Resolved Cell Atlas of the Whole Mouse Brain.” *Nature* 624 (7991): 343–54. https://doi.org/10.1038/s41586-023-06808-9.

Zhang, Xiuli, Lingna Lv, Qian Chen, et al. 2013. “Mouse DNA Polymerase Kappa Has a Functional Role in the Repair of DNA Strand Breaks.” *DNA Repair* 12 (5): 377–88. https://doi.org/10.1016/j.dnarep.2013.02.008.

Zhang, Y., F. Yuan, X. Wu, et al. 2000. “Error-Free and Error-Prone Lesion Bypass by Human DNA Polymerase Kappa in Vitro.” *Nucleic Acids Research* 28 (21): 21. https://doi.org/10.1093/nar/28.21.4138.

Zhuo, Ming, Murat F. Gorgun, and Ella W. Englander. 2018. “Translesion Synthesis DNA Polymerase Kappa Is Indispensable for DNA Repair Synthesis in Cisplatin Exposed Dorsal Root Ganglion Neurons.” *Molecular Neurobiology* 55 (3): 2506–15. https://doi.org/10.1007/s12035-017-0507-5.

Figure 1

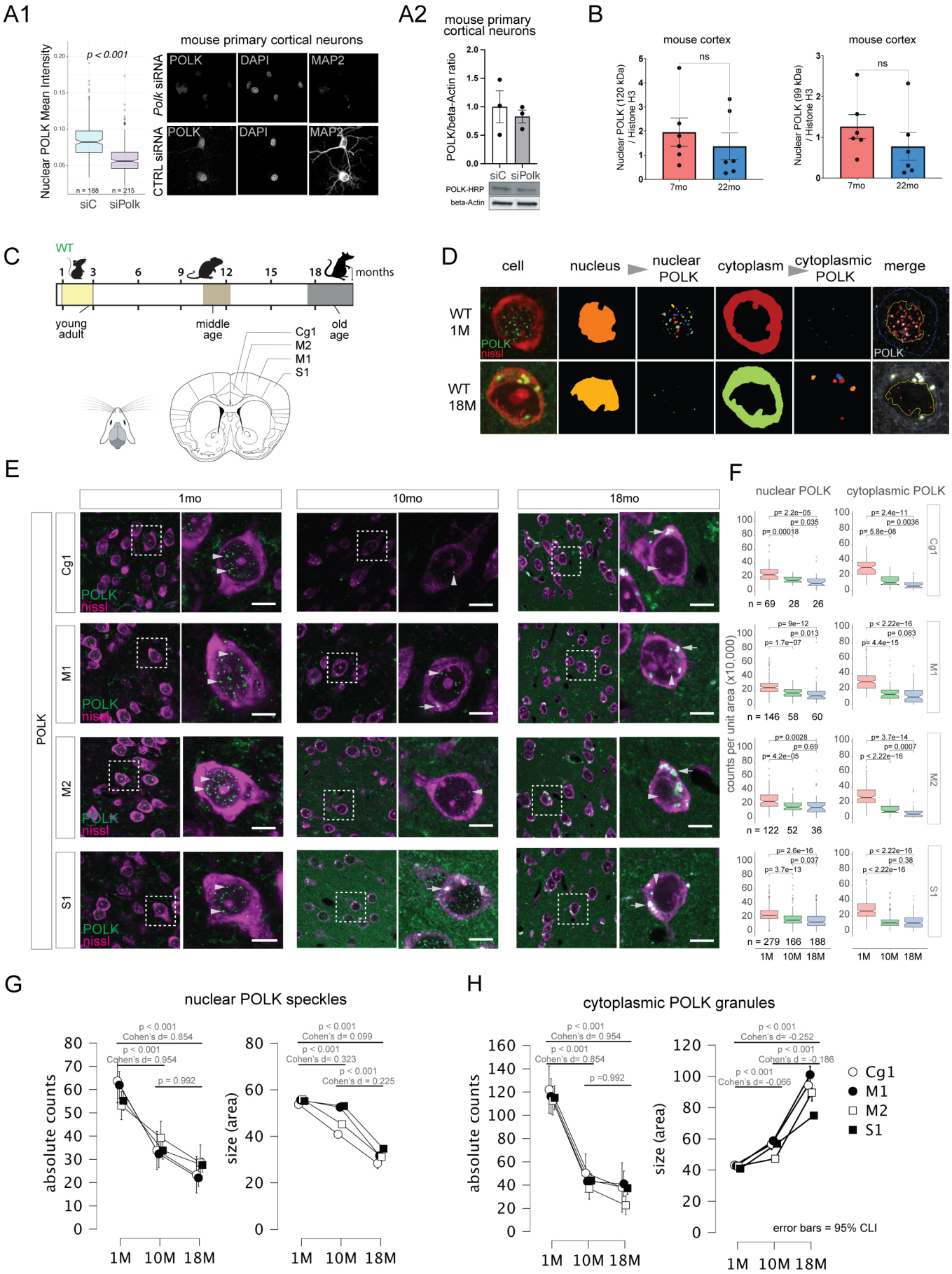
A1
mouse primary cortical neurons
Nuclear POLK Mean Intensity
p < 0.001
n = 188
n = 215
siC
siPolk
Polk siRNA
CTRL siRNA
POLK
DAPI
MAP2
A2
mouse primary cortical neurons
POLK/beta-Actin ratio
siC
siPolk
POLK-HRP
beta-Actin
B
mouse cortex
Nuclear POLK (120 kDa) / Histone H3
Nuclear POLK (99 kDa) / Histone H3
ns
7mo
22mo
C
WT
months
young adult
middle age
old age
Cg1
M2
M1
S1
D
cell
nucleus
nuclear POLK
cytoplasm
cytoplasmic POLK
merge
WT 1M
WT 18M
POLK
nissl
E
1mo
10mo
18mo
POLK
Cg1
M1
M2
S1
F
nuclear POLK
cytoplasmic POLK
counts per unit area (x10,000)
n = 69 28 26
n = 146 58 60
n = 122 52 36
n = 279 166 188
1M 10M 18M
G
nuclear POLK speckles
absolute counts
size (area)
p < 0.001
Cohen's d= 0.854
p < 0.001
Cohen's d= 0.954
p = 0.992
p < 0.001
Cohen's d= 0.099
p < 0.001
Cohen's d= 0.323
p < 0.001
Cohen's d = 0.225
1M 10M 18M
H
cytoplasmic POLK granules
absolute counts
size (area)
p < 0.001
Cohen's d= 0.954
p < 0.001
Cohen's d= 0.854
p =0.992
p < 0.001
Cohen's d= -0.252
p < 0.001
Cohen's d = -0.186
p < 0.001
Cohen's d= -0.066
Cg1
M1
M2
S1
error bars = 95% CLI
1M 10M 18M

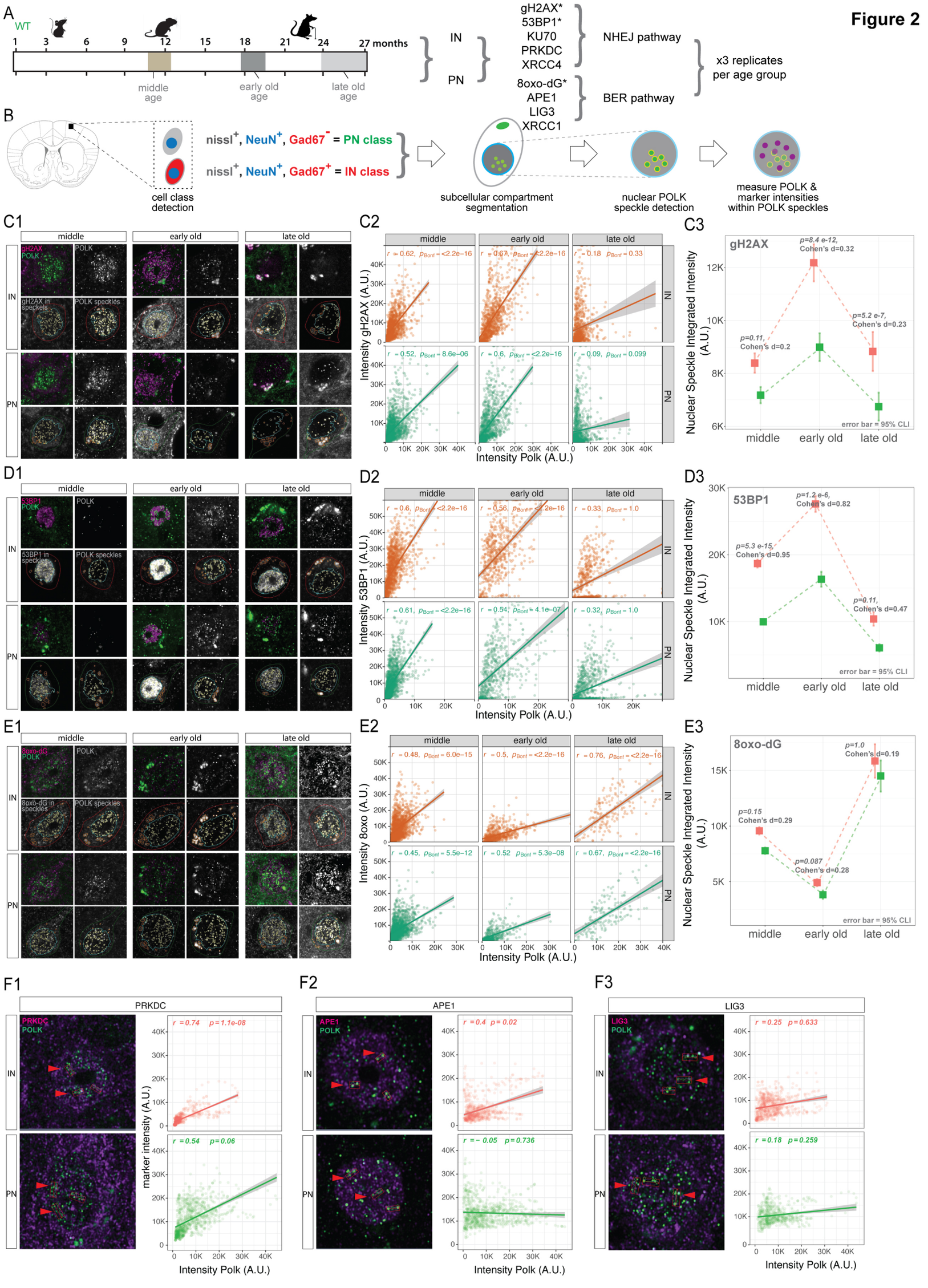
Figure 2
A
WT
1 3 6 9 12 15 18 21 24 27 months
middle age
early old age
late old age
IN
PN
gH2AX*
53BP1*
KU70
PRKDC
XRCC4
NHEJ pathway
8oxo-dG*
APE1
LIG3
XRCC1
BER pathway
x3 replicates per age group
B
nissl+, NeuN+, Gad67- = PN class
nissl+, NeuN+, Gad67+ = IN class
cell class detection
subcellular compartment segmentation
nuclear POLK speckle detection
measure POLK & marker intensities within POLK speckles
C1
middle
early old
late old
gH2AX
POLK
gH2AX in speckels
POLK speckles
IN
PN
C2
Intensity gH2AX (A.U.)
Intensity Polk (A.U.)
C3
gH2AX
p=8.4 e-12, Cohen's d=0.32
p=5.2 e-7, Cohen's d=0.23
p=0.11, Cohen's d=0.2
error bar = 95% CLI
Nuclear Speckle Integrated Intensity (A.U.)
D1
53BP1
53BP1 in speckles
D2
Intensity 53BP1 (A.U.)
D3
53BP1
p=1.2 e-6, Cohen's d=0.82
p=5.3 e-15, Cohen's d=0.95
p=0.11, Cohen's d=0.47
E1
8oxo-dG
8oxo-dG in speckles
E2
Intensity 8oxo (A.U.)
E3
8oxo-dG
p=1.0 Cohen's d=0.19
p=0.15 Cohen's d=0.29
p=0.087 Cohen's d=0.28
F1
PRKDC
r = 0.74 p = 1.1e-08
r = 0.54 p = 0.06
marker intensity (A.U.)
F2
APE1
r = 0.4 p = 0.02
r = − 0.05 p = 0.736
F3
LIG3
r = 0.25 p = 0.633
r = 0.18 p = 0.259

Figure 3

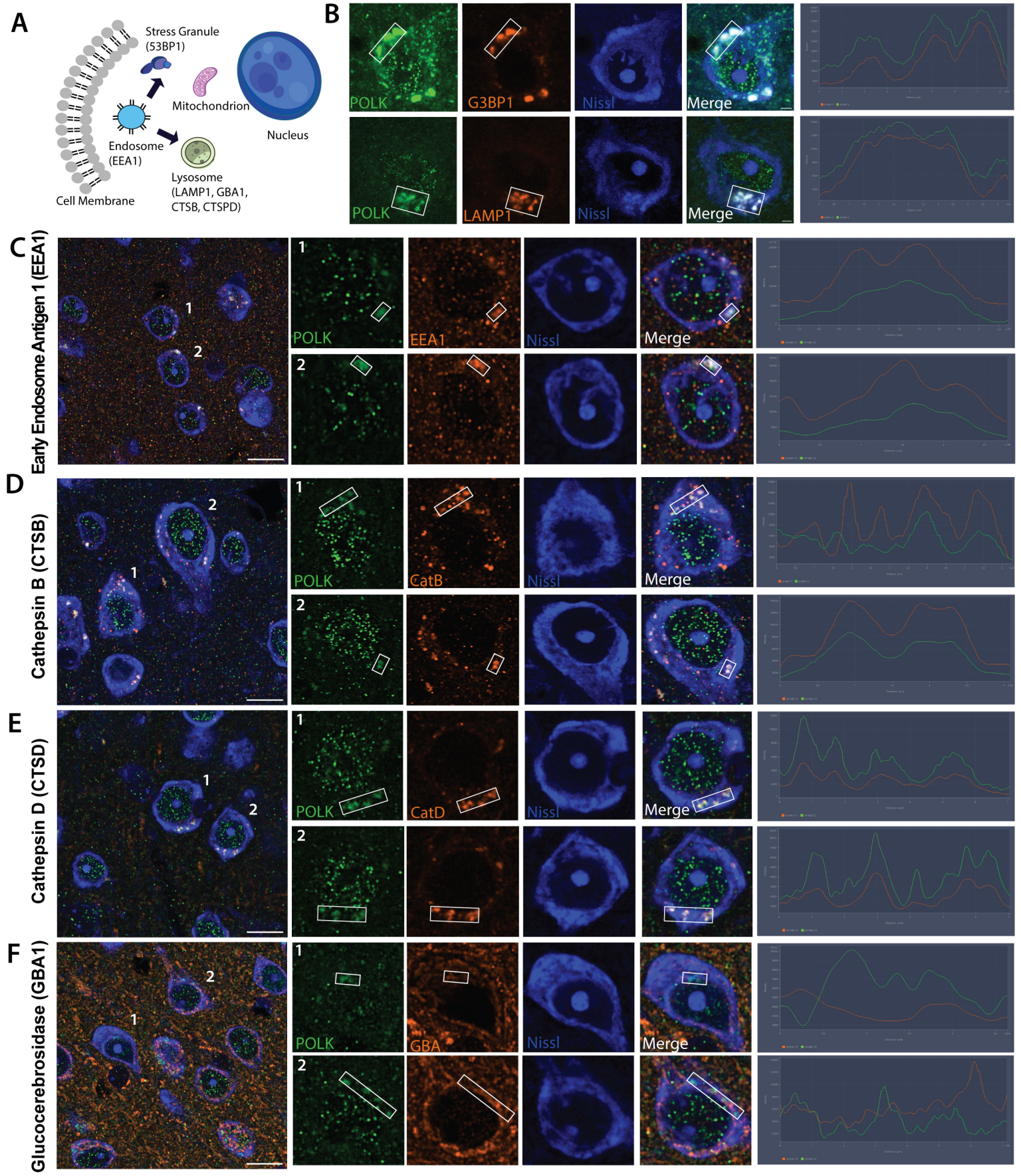
A
Stress Granule
(53BP1)
Mitochondrion
Nucleus
Endosome
(EEA1)
Lysosome
(LAMP1, GBA1,
CTSB, CTSPD)
Cell Membrane
B
POLK
G3BP1
Nissl
Merge
POLK
LAMP1
Nissl
Merge
C
Early Endosome Antigen 1 (EEA1)
1
2
POLK
EEA1
Nissl
Merge
D
Cathepsin B (CTSB)
POLK
CatB
Nissl
Merge
E
Cathepsin D (CTSD)
POLK
CatD
Nissl
Merge
F
Glucocerebrosidase (GBA1)
POLK
GBA
Nissl
Merge

Figure 4

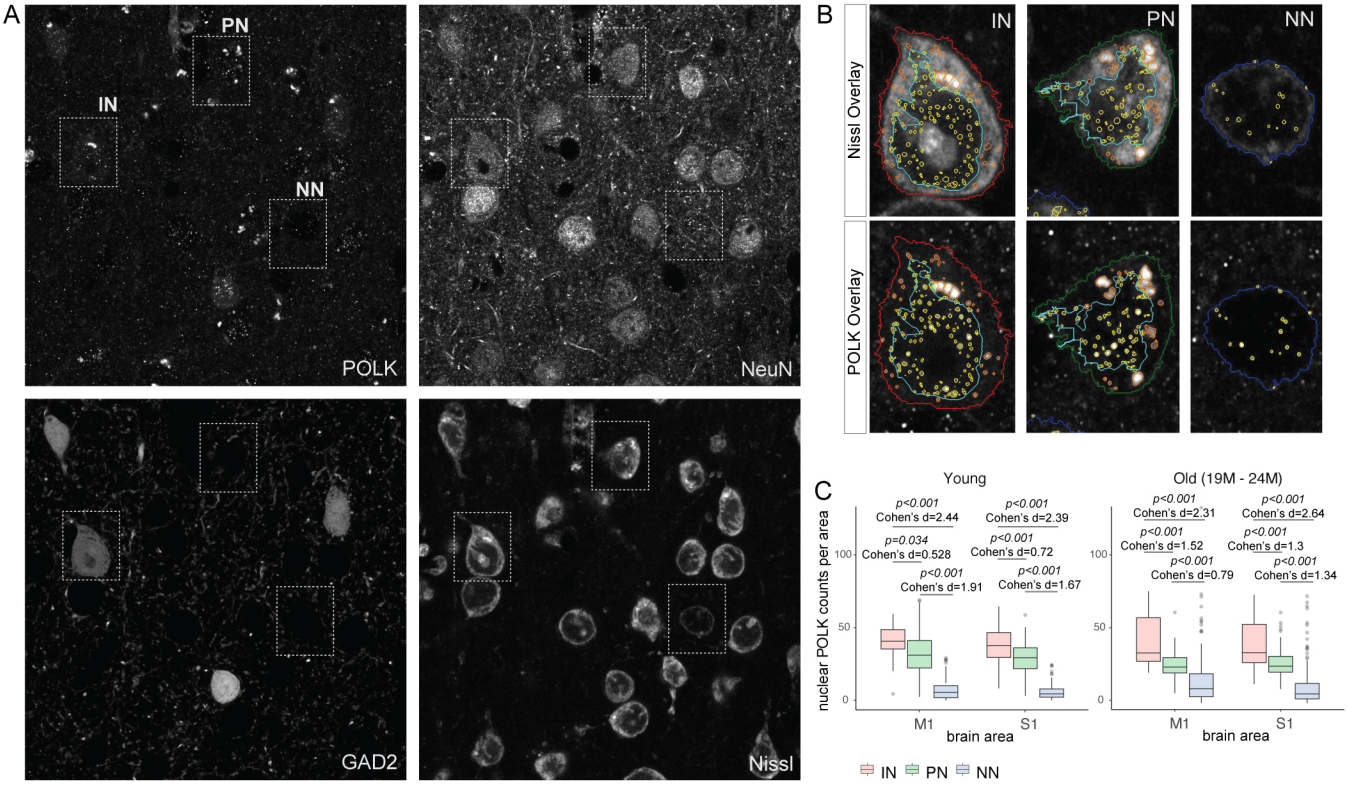
A
PN
IN
NN
POLK
NeuN
GAD2
Nissl
B
Nissl Overlay
POLK Overlay
IN
PN
NN
C
Young
Old (19M - 24M)
nuclear POLK counts per area
p<0.001
Cohen's d=2.44
p=0.034
Cohen's d=0.528
p<0.001
Cohen's d=1.91
p<0.001
Cohen's d=2.39
p<0.001
Cohen's d=0.72
p<0.001
Cohen's d=1.67
p<0.001
Cohen's d=2.31
p<0.001
Cohen's d=1.52
p<0.001
Cohen's d=0.79
p<0.001
Cohen's d=2.64
p<0.001
Cohen's d=1.3
p<0.001
Cohen's d=1.34
100
50
0
M1
S1
brain area
IN
PN
NN

Figure 5

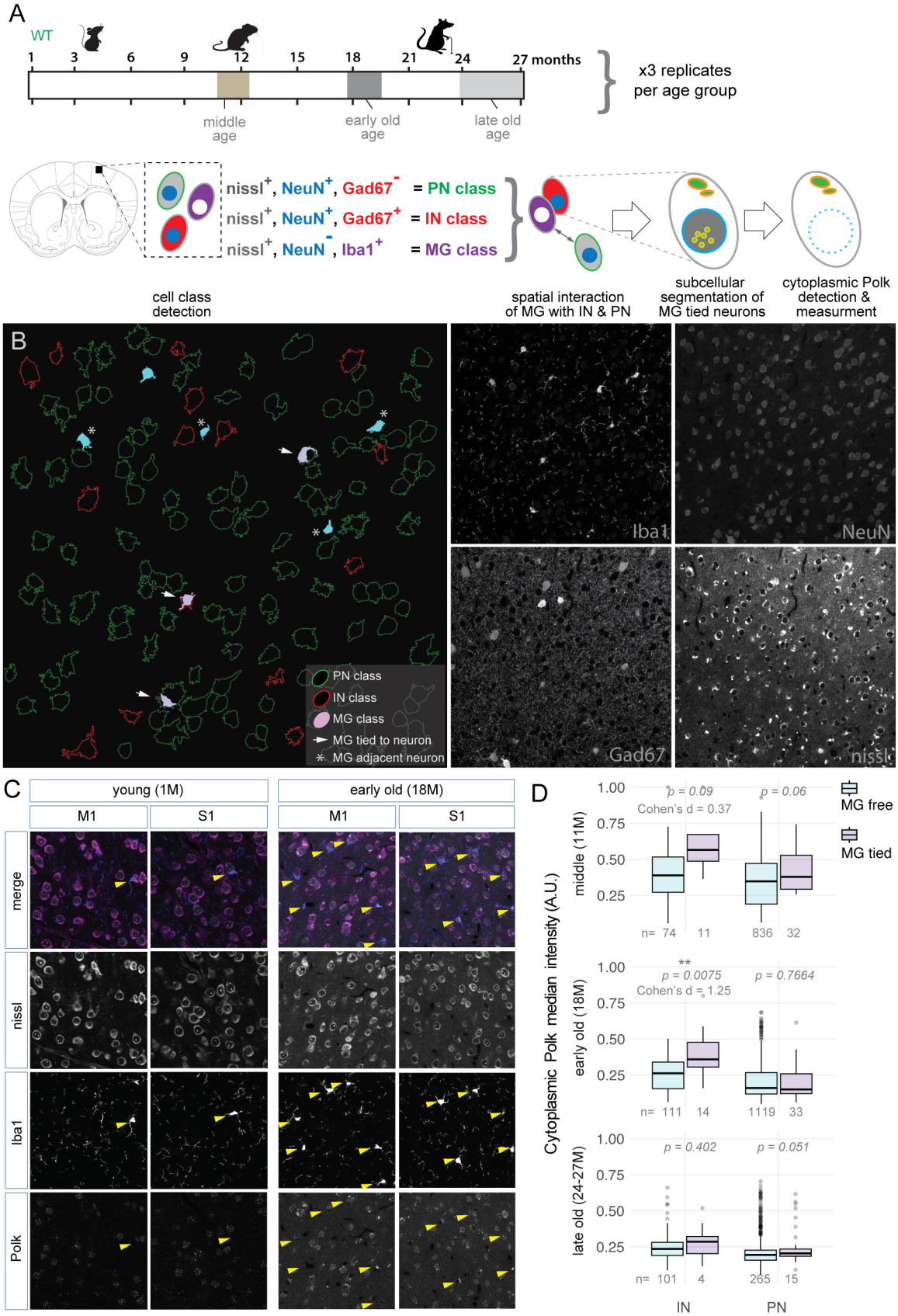
A
WT
1
3
6
9
12
15
18
21
24
27 months
middle age
early old age
late old age
x3 replicates per age group
nissl+, NeuN+, Gad67- = PN class
nissl+, NeuN+, Gad67+ = IN class
nissl+, NeuN-, Iba1+ = MG class
cell class detection
spatial interaction of MG with IN & PN
subcellular segmentation of MG tied neurons
cytoplasmic Polk detection & measurment
B
PN class
IN class
MG class
MG tied to neuron
MG adjacent neuron
Iba1
NeuN
Gad67
nissl
C
young (1M)
early old (18M)
M1
S1
merge
nissl
Iba1
Polk
D
Cytoplasmic Polk median intensity (A.U.)
middle (11M)
early old (18M)
late old (24-27M)
p = 0.09
Cohen's d = 0.37
p = 0.06
n= 74
11
836
32
**
p = 0.0075
Cohen's d = 1.25
p = 0.7664
n= 111
14
1119
33
p = 0.402
p = 0.051
n= 101
4
265
15
IN
PN
MG free
MG tied

Figure 6

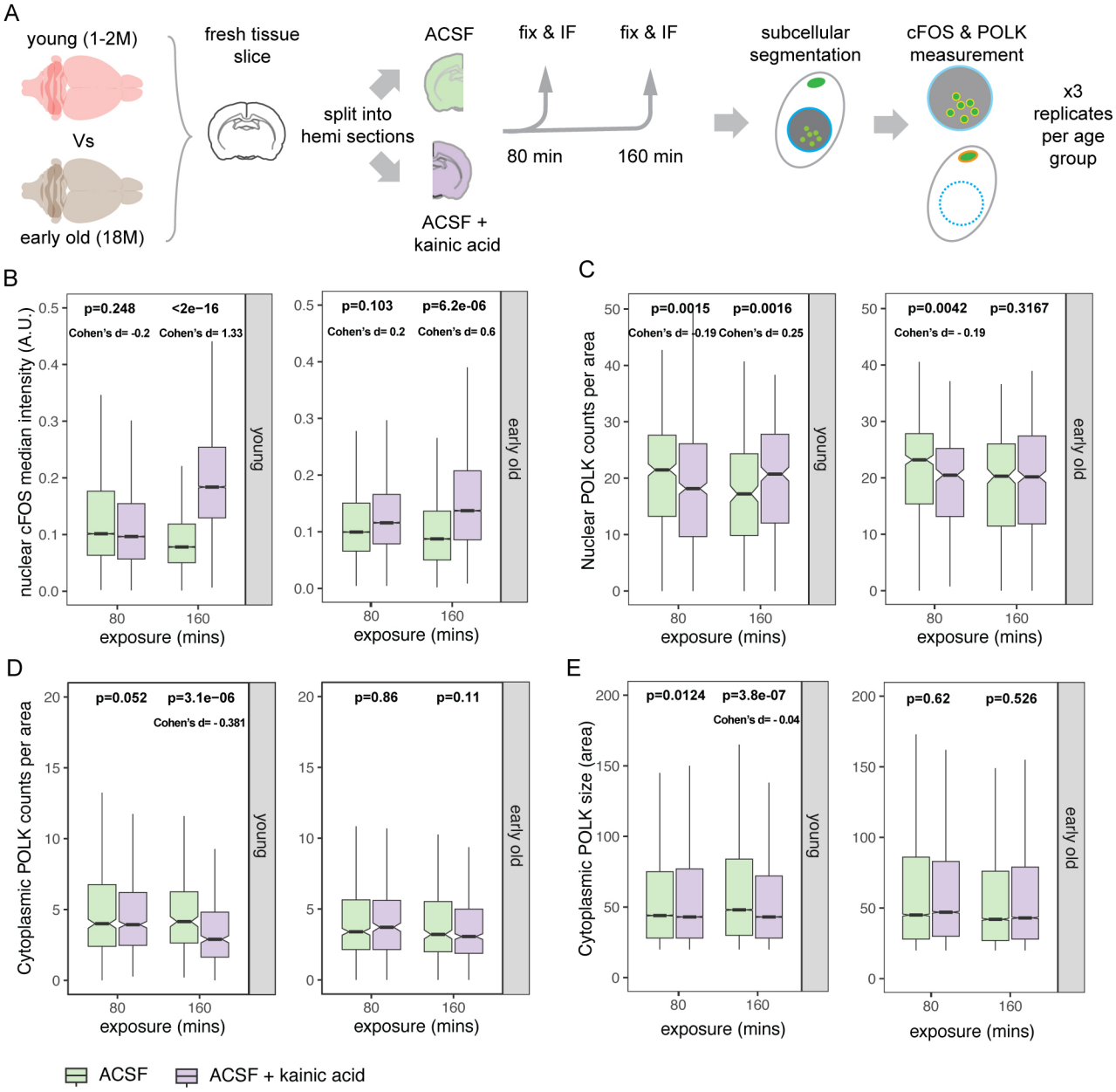
A
young (1-2M)
Vs
early old (18M)
fresh tissue slice
split into hemi sections
ACSF
ACSF + kainic acid
fix & IF
fix & IF
80 min
160 min
subcellular segmentation
cFOS & POLK measurement
x3 replicates per age group
B
nuclear cFOS median intensity (A.U.)
p=0.248
<2e−16
Cohen's d= -0.2
Cohen's d= 1.33
p=0.103
p=6.2e-06
Cohen's d= 0.2
Cohen's d= 0.6
young
early old
exposure (mins)
C
Nuclear POLK counts per area
p=0.0015
p=0.0016
Cohen's d= -0.19
Cohen's d= 0.25
p=0.0042
p=0.3167
Cohen's d= - 0.19
D
Cytoplasmic POLK counts per area
p=0.052
p=3.1e−06
Cohen's d= - 0.381
p=0.86
p=0.11
E
Cytoplasmic POLK size (area)
p=0.0124
p=3.8e-07
Cohen's d= - 0.04
p=0.62
p=0.526
ACSF
ACSF + kainic acid

Figure 7

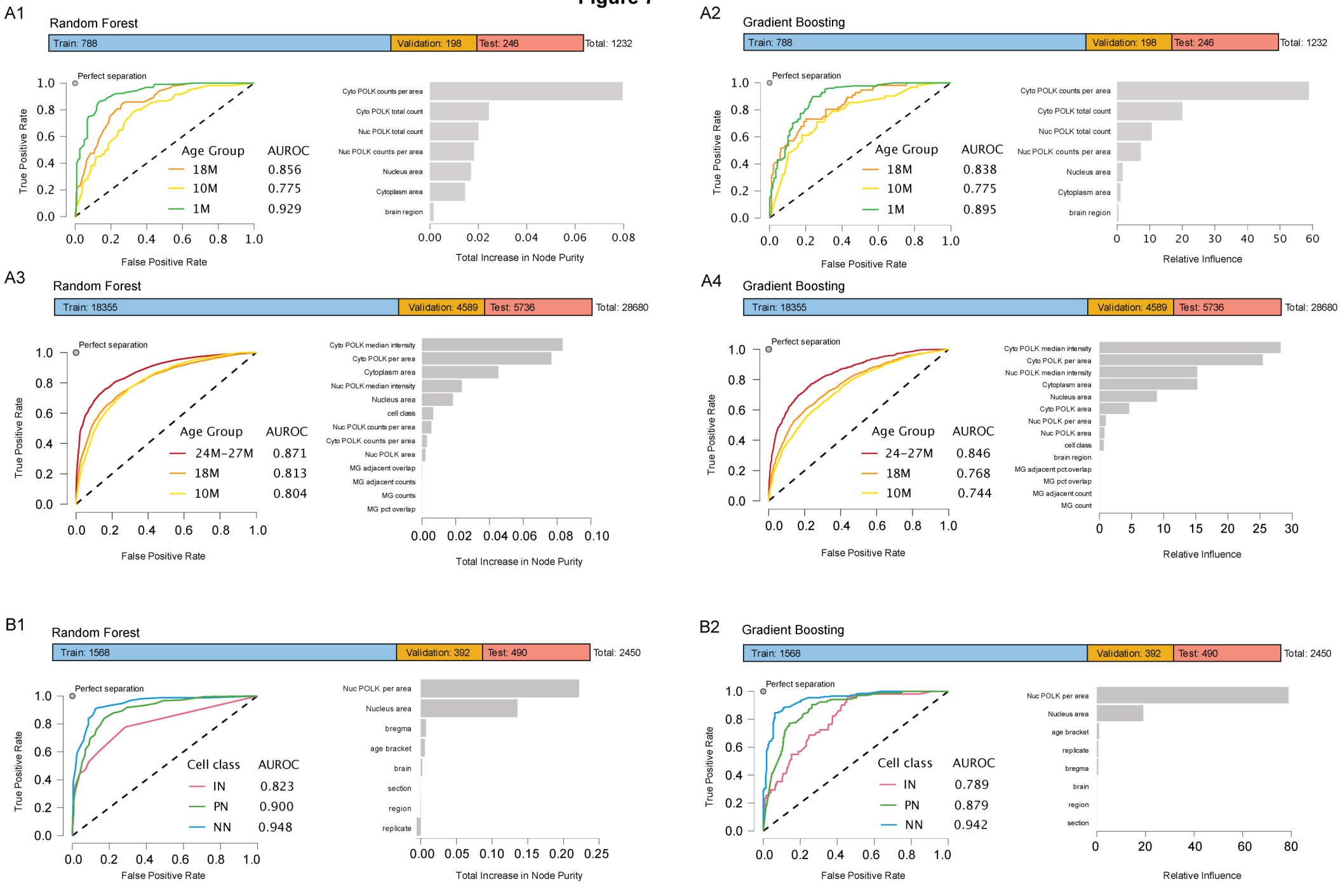
A1
Random Forest
Train: 788
Validation: 198
Test: 246
Total: 1232
Perfect separation
True Positive Rate
False Positive Rate
Age Group
AUROC
18M 0.856
10M 0.775
1M 0.929
Cyto POLK counts per area
Cyto POLK total count
Nuc POLK total count
Nuc POLK counts per area
Nucleus area
Cytoplasm area
brain region
Total Increase in Node Purity
A2
Gradient Boosting
Train: 788
Validation: 198
Test: 246
Total: 1232
Perfect separation
True Positive Rate
False Positive Rate
Age Group
AUROC
18M 0.838
10M 0.775
1M 0.895
Cyto POLK counts per area
Cyto POLK total count
Nuc POLK total count
Nuc POLK counts per area
Nucleus area
Cytoplasm area
brain region
Relative Influence
A3
Random Forest
Train: 18355
Validation: 4589
Test: 5736
Total: 28680
Perfect separation
True Positive Rate
False Positive Rate
Age Group
AUROC
24M–27M 0.871
18M 0.813
10M 0.804
Cyto POLK median intensity
Cyto POLK per area
Cytoplasm area
Nuc POLK median intensity
Nucleus area
cell class
Nuc POLK counts per area
Cyto POLK counts per area
Nuc POLK area
MG adjacent overlap
MG adjacent counts
MG counts
MG pct overlap
Total Increase in Node Purity
A4
Gradient Boosting
Train: 18355
Validation: 4589
Test: 5736
Total: 28680
Perfect separation
True Positive Rate
False Positive Rate
Age Group
AUROC
24–27M 0.846
18M 0.768
10M 0.744
Cyto POLK median intensity
Cyto POLK per area
Nuc POLK median intensity
Cytoplasm area
Nucleus area
Cyto POLK area
Nuc POLK per area
Nuc POLK area
cell class
brain region
MG adjacent pct.overlap
MG pct overlap
MG adjacent count
MG count
Relative Influence
B1
Random Forest
Train: 1568
Validation: 392
Test: 490
Total: 2450
Perfect separation
True Positive Rate
False Positive Rate
Cell class
AUROC
IN 0.823
PN 0.900
NN 0.948
Nuc POLK per area
Nucleus area
bregma
age bracket
brain
section
region
replicate
Total Increase in Node Purity
B2
Gradient Boosting
Train: 1568
Validation: 392
Test: 490
Total: 2450
Perfect separation
True Positive Rate
False Positive Rate
Cell class
AUROC
IN 0.789
PN 0.879
NN 0.942
Nuc POLK per area
Nucleus area
age bracket
replicate
bregma
brain
region
section
Relative Influence

Supplement Figure S1 associated with Figure 1

S1A

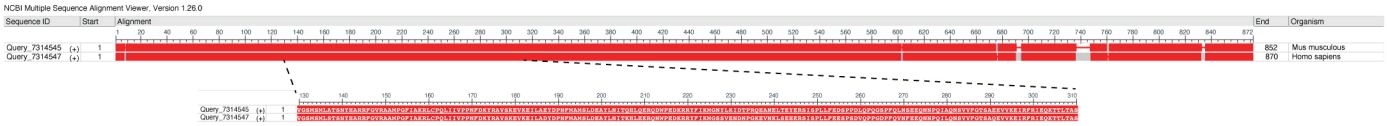

S1B

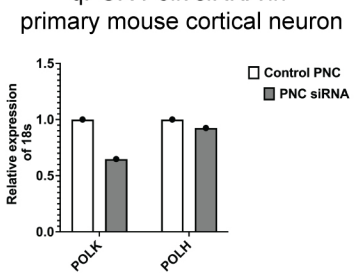

S1C

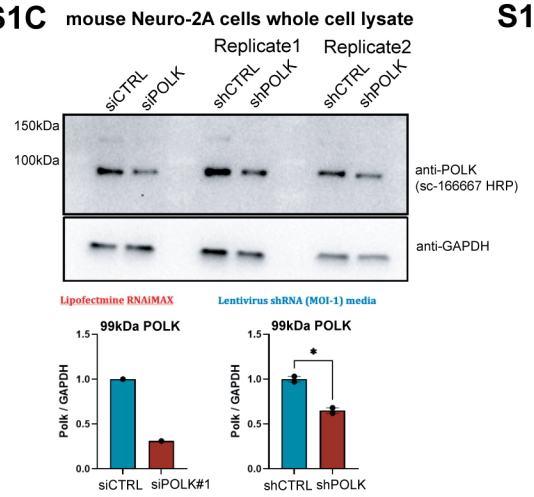

S1D

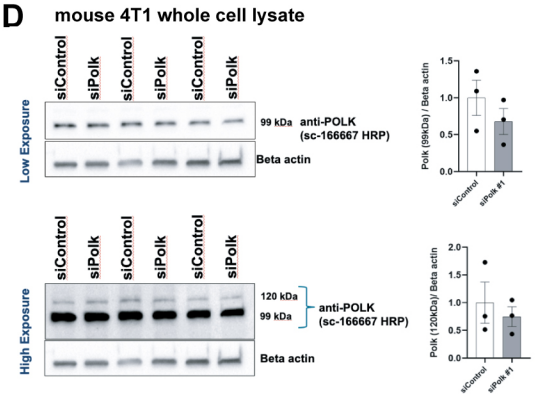

S1E

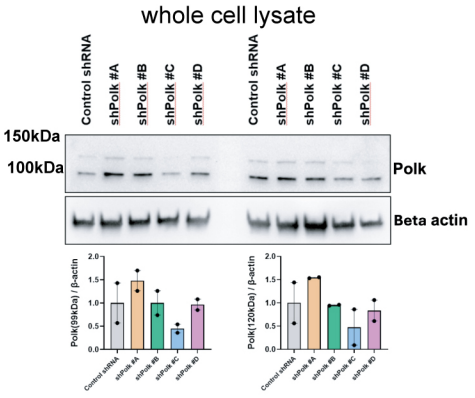

S1F

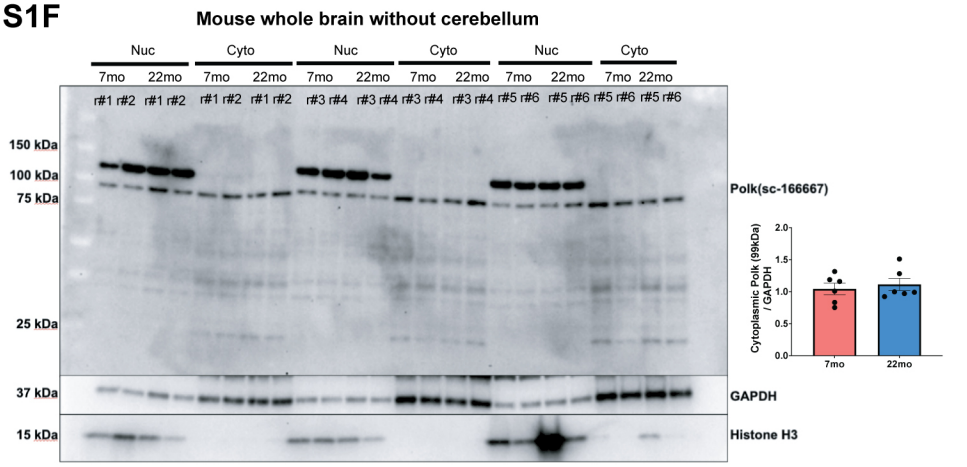

S1G

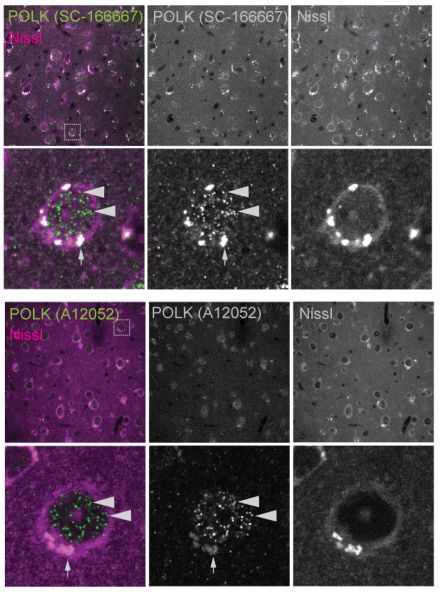

S1H

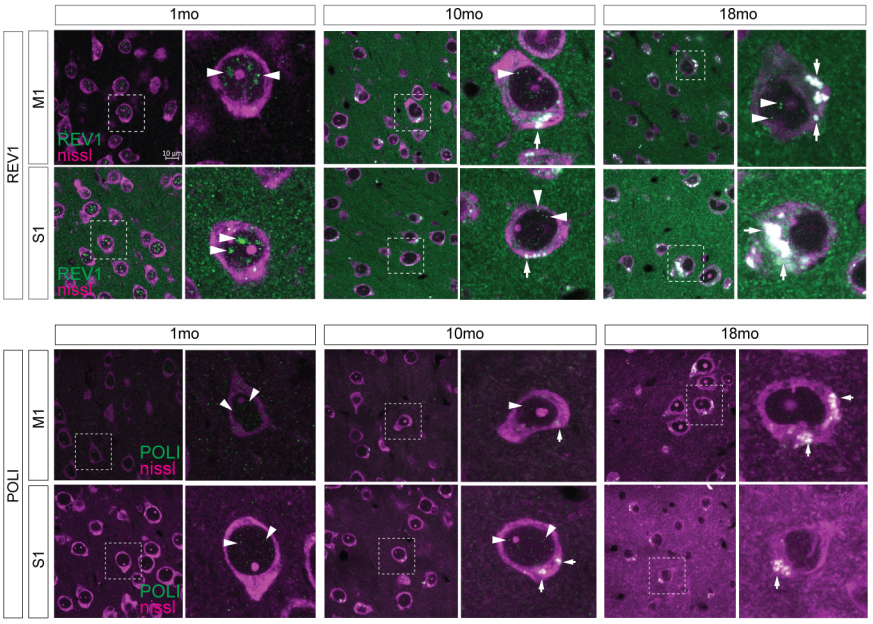

Supplement Figure S2 associated with Figure 2

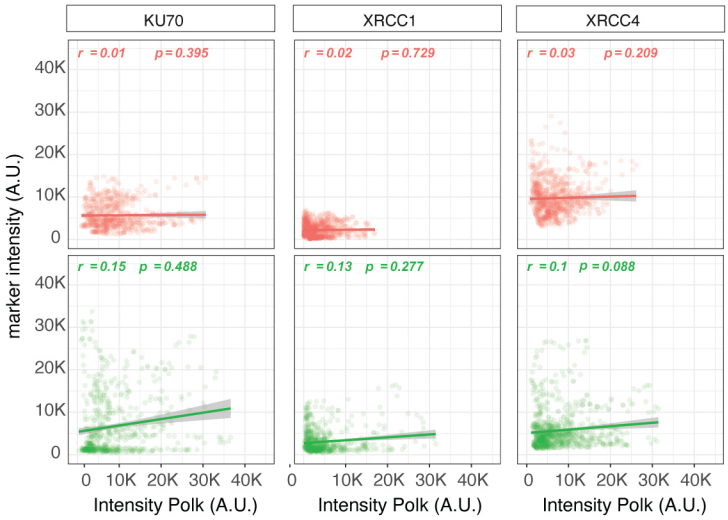

Figure S3 Supplement to Figure 3

S3A

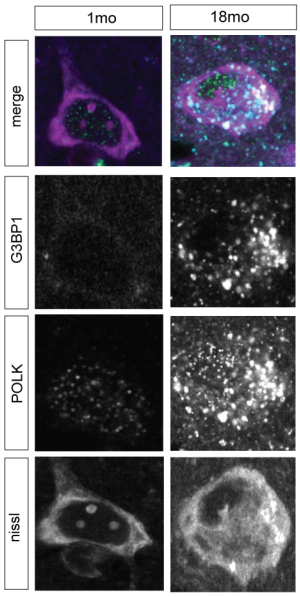

S3B

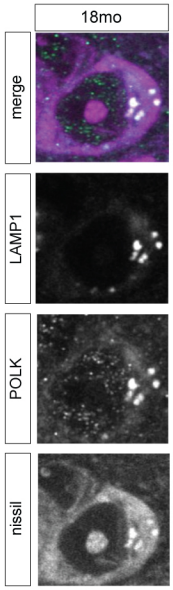

S3C Wild type 18 month brain, cortical area S1

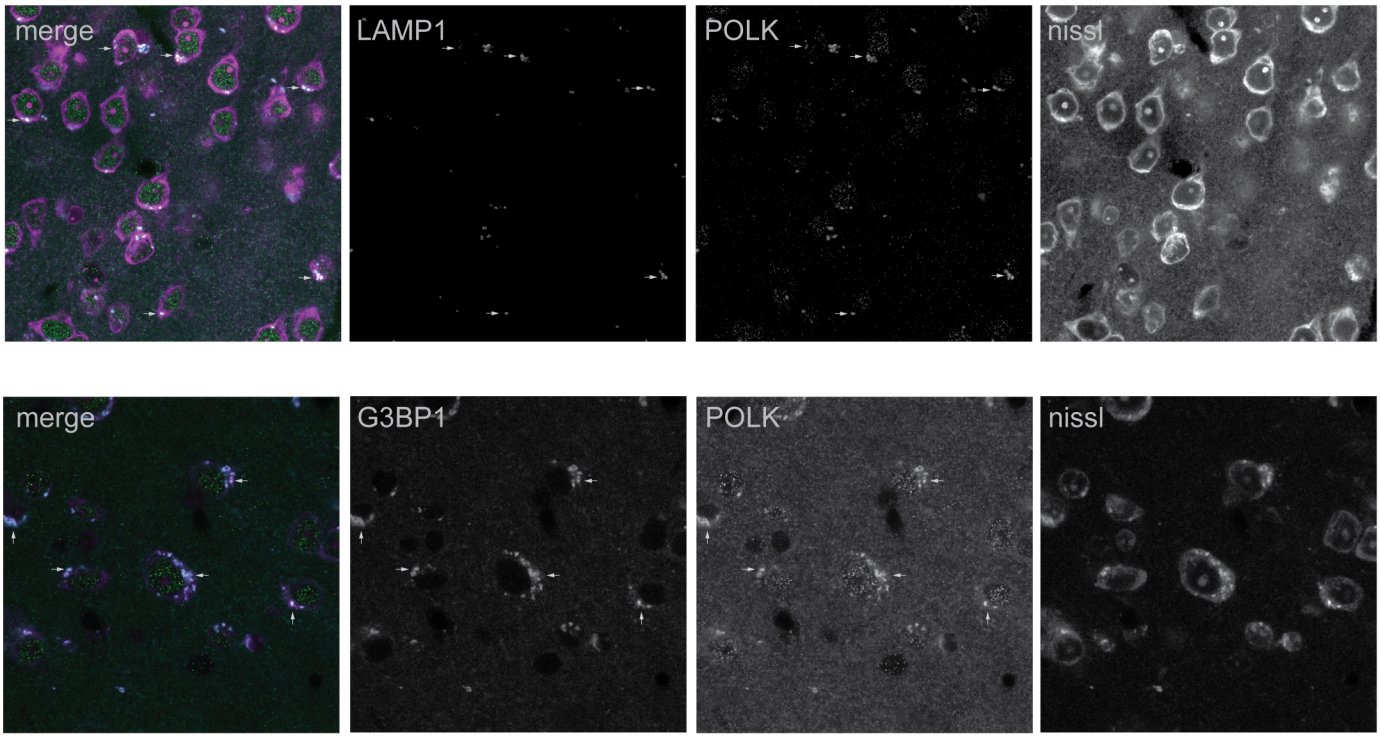

Supplement Figure S4 associated with Figure 5

S4

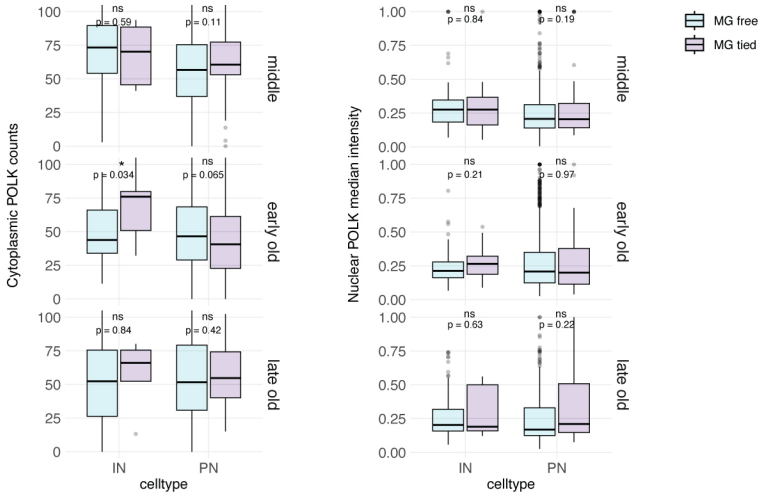

Figure S5: Supplement of Figure 6

S5A Nuclear cFOS median intensity (A.U.)

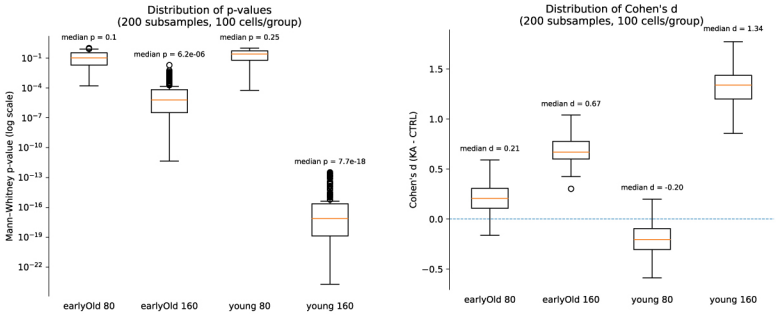

Fig 6B. Distribution of p values and Cohen's d values after subsampling 200 times with 100cells/group

age_grp	exposure	comparison	p_min	p_25	p_median	p_75	p_max	d_min	d_25	d_median	d_75	d_max
early old	80	KA-CTRL	0.00015998	0.01930747	0.10343143	0.33585548	0.99122724	-0.1632298	0.10740943	0.2063694	0.30701467	0.59148485
early old	160	KA-CTRL	4.4878E-12	3.2606E-07	6.2182E-06	6.6773E-05	0.01930721	0.30239053	0.60015085	0.66966879	0.77668113	1.04029956
young	80	KA-CTRL	5.6858E-05	0.06004031	0.24804876	0.53226951	0.99220195	-0.5873628	-0.3049781	-0.2035	-0.0950161	0.19863244
young	160	KA-CTRL	1.9349E-24	1.3586E-19	7.6995E-18	2.3434E-16	3.3362E-13	0.8569429	1.19984392	1.33968492	1.43648131	1.7729879

S5B Cytoplasmic POLK size (area)

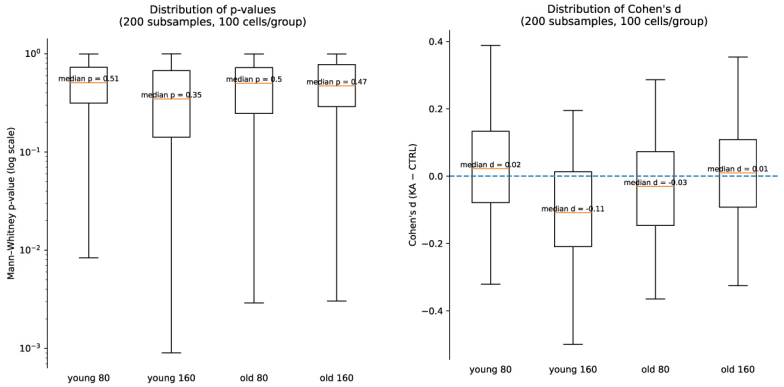

Fig 6E. Distribution of p values and Cohen's d values after subsampling 200 times with 100cells/group

age_grp	exposure	comparison	p_min	p_25	p_median	p_75	p_max	d_min	d_25	d_median	d_75	d_max
early old	80	KA-CTRL	0.00290041	0.24641209	0.50077205	0.72169723	0.99512498	-0.3647349	-0.1464119	-0.0307934	0.07286557	0.28622058
early old	160	KA-CTRL	0.00303319	0.28979697	0.47089391	0.77678619	0.99512498	-0.3251215	-0.0918906	0.00966706	0.10842447	0.3536342
young	80	KA-CTRL	0.00836628	0.3142806	0.50852219	0.72761533	0.99414989	-0.3208024	-0.0787673	0.02197868	0.13300206	0.38851313
young	160	KA-CTRL	0.00089957	0.14148282	0.34674382	0.67174843	0.99707503	-0.4996196	-0.209243	-0.1088372	0.01291603	0.1948351

Absolute counts of nuclear Polk speckles

Table 1.1

ANCOVA Post Hoc Comparisons - age, with nuclear area as covariate

		Mean Diff	SE	t	Cohen's d	p_{tukey}		p_{bonf}	
1M	10M	18.432	1.806	10.203	0.854	< .001	***	< .001	***
1M	18M	20.584	1.918	10.733	0.954	< .001	***	< .001	***
10M	18M	2.152	2.212	0.973	0.1	0.594		0.992	

Note. Results are averaged over the levels of: brain area
Note. P-value adjusted for comparing a family of 3
* p < .05, ** p < .01, *** p < .001

Table 1.2

ANCOVA Post Hoc Comparisons - age ∗ brain area, with nuclear area as covariate

		Mean Diff	SE	t	Cohen's d	p_{tukey}		p_{bonf}	
1M Cg1	10M Cg1	22.276	4.841	4.602	1.032	< .001	***	< .001	***
1M Cg1	18M Cg1	25.265	4.987	5.066	1.171	< .001	***	< .001	***
10M Cg1	18M Cg1	2.99	5.881	0.508	0.139	1		1	
1M M1	10M M1	18.729	3.366	5.564	0.868	< .001	***	< .001	***
1M M1	18M M1	24.795	3.341	7.421	1.149	< .001	***	< .001	***
10M M1	18M M1	6.066	3.976	1.526	0.281	0.933		1	
1M M2	10M M2	17.852	3.576	4.992	0.827	< .001	***	< .001	***
1M M2	18M M2	14.258	4.105	3.474	0.661	0.026	*	0.035	*
10M M2	18M M2	-3.593	4.699	-0.765	-0.167	1		1	
1M S1	10M S1	14.873	2.117	7.027	0.689	< .001	***	< .001	***
1M S1	18M S1	18.018	2.057	8.758	0.835	< .001	***	< .001	***
10M S1	18M S1	3.144	2.293	1.371	0.146	0.969		1	

Note. P-value adjusted for comparing a family of 12, only relevant comparisons are shown
* p < .05, ** p < .01, *** p < .001

Size (area) of nuclear Polk speckles

Table 2.1

ANOVA Post Hoc Comparisons - age

		Mean Differen	SE	t	Cohen's d	p_{tukey}		p_{bonf}	
1M	10M	7.195	0.431	16.708	0.099	< .001	***	< .001	***
1M	18M	23.617	0.578	40.861	0.323	< .001	***	< .001	***
10M	18M	16.422	0.653	25.143	0.225	< .001	***	< .001	***

Note. Results are averaged over the levels of: brain area
Note. P-value adjusted for comparing a family of 3
* p < .05, ** p < .01, *** p < .001

Table 2.2

ANOVA Post Hoc Comparisons - age ∗ area

		Mean Diff	SE	t	Cohen's d	p_{tukey}		p_{bonf}	
1M Cg1	10M Cg1	12.882	1.11	11.6	0.176	< .001	***	< .001	***
1M Cg1	18M Cg1	25.397	1.534	16.56	0.348	< .001	***	< .001	***
10M Cg1	18M Cg1	12.516	1.714	7.304	0.171	< .001	***	< .001	***
1M M1	10M M1	3.105	0.877	3.542	0.043	0.02	*	0.026	*
1M M1	18M M1	23.945	1.035	23.125	0.328	< .001	***	< .001	***
10M M1	18M M1	20.841	1.248	16.697	0.285	< .001	***	< .001	***
1M M2	10M M2	10.629	0.805	13.196	0.146	< .001	***	< .001	***
1M M2	18M M2	24.644	1.263	19.512	0.338	< .001	***	< .001	***
10M M2	18M M2	14.015	1.365	10.27	0.192	< .001	***	< .001	***
1M S1	10M S1	2.165	0.563	3.847	0.03	0.007	**	0.008	**
1M S1	18M S1	20.483	0.571	35.892	0.281	< .001	***	< .001	***
10M S1	18M S1	18.318	0.685	26.749	0.251	< .001	***	< .001	***

Note. P-value adjusted for comparing a family of 12, only relevant comparisons are shown
* p < .05, ** p < .01, *** p < .001

Absolute counts of cytoplasmic Polk granules

Table 3.1

Post Hoc Comparisons - age, with cytoplasmic area as covariate

		Mean Diff	SE	t	Cohen's d	p_{tukey}		p_{bonf}	
1M	10M	18.432	1.806	10.203	0.854	< .001	***	< .001	***
1M	18M	20.584	1.918	10.733	0.954	< .001	***	< .001	***
10M	18M	2.152	2.212	0.973	0.1	0.594		0.992	

Note. Results are averaged over the levels of: brain area
Note. P-value adjusted for comparing a family of 3
* p < .05, ** p < .01, *** p < .001

Table 3.2

ANCOVA Post Hoc Comparisons - age ∗ brain area, with cytoplasmic area as covariate

		Mean Diff	SE	t	Cohen's d	p_{tukey}		p_{bonf}	
1M Cg1	10M Cg1	57.944	10.232	5.663	1.27	< .001	***	< .001	***
1M Cg1	18M Cg1	80.174	10.502	7.634	1.757	< .001	***	< .001	***
10M Cg1	18M Cg1	22.23	12.432	1.788	0.487	0.824		1	
1M M1	10M M1	59.109	7.094	8.333	1.295	< .001	***	< .001	***
1M M1	18M M1	60.769	7.009	8.67	1.332	< .001	***	< .001	***
10M M1	18M M1	1.661	8.403	0.198	0.036	1		1	
1M M2	10M M2	58.471	7.572	7.722	1.281	< .001	***	< .001	***
1M M2	18M M2	66.588	8.679	7.672	1.459	< .001	***	< .001	***
10M M2	18M M2	8.117	9.896	0.82	0.178	1		1	
1M S1	10M S1	60.836	4.466	13.623	1.333	< .001	***	< .001	***
1M S1	18M S1	57.122	4.343	13.153	1.252	< .001	***	< .001	***
10M S1	18M S1	-3.713	4.853	-0.765	-0.081	1		1	

Note. P-value adjusted for comparing a family of 12, only relevant comparisons are shown
* p < .05, ** p < .01, *** p < .001

Size (area) of cytoplasmic Polk granules

Table 4.1

Post Hoc Comparisons - age

		Mean Diff	SE	t	Cohen's d	p_{tukey}		p_{bonf}	
1M	10M	-12.531	0.667	-18.778	-0.066	< .001	***	< .001	***
1M	18M	-47.599	0.904	-52.653	-0.252	< .001	***	< .001	***
10M	18M	-35.068	1.036	-33.834	-0.186	< .001	***	< .001	***

Note. Results are averaged over the levels of: area
Note. P-value adjusted for comparing a family of 3
*** p < .001

Table 4.2

Post Hoc Comparisons - age ∗ area

		Mean Diff	SE	t	Cohen's d	p_{tukey}		p_{bonf}	
1M Cg1	10M Cg1	-13.423	1.666	-8.057	-0.071	< .001	***	< .001	***
1M Cg1	18M Cg1	-51.086	2.545	-20.074	-0.27	< .001	***	< .001	***
10M Cg1	18M Cg1	-37.662	2.845	-13.236	-0.199	< .001	***	< .001	***
1M M1	10M M1	-16.06	1.382	-11.619	-0.085	< .001	***	< .001	***
1M M1	18M M1	-58.375	1.472	-39.662	-0.309	< .001	***	< .001	***
10M M1	18M M1	-42.314	1.853	-22.832	-0.224	< .001	***	< .001	***
1M M2	10M M2	-4.69	1.308	-3.585	-0.025	0.018	*	0.022	*
1M M2	18M M2	-46.978	1.951	-24.076	-0.249	< .001	***	< .001	***
10M M2	18M M2	-42.288	2.164	-19.544	-0.224	< .001	***	< .001	***
1M S1	10M S1	-15.95	0.853	-18.698	-0.084	< .001	***	< .001	***
1M S1	18M S1	-33.958	0.791	-42.926	-0.18	< .001	***	< .001	***
10M S1	18M S1	-18.008	0.988	-18.231	-0.095	< .001	***	< .001	***

Note. P-value adjusted for comparing a family of 12, only relevant comparisons are shown
* p < .05, ** p < .01, *** p < .001

Table 5.1

Cell class nuclear Polk counts per area

Post Hoc Comparisons - age_bracket ∗ Cell-type

		Mean Diff	SE	t	Cohen's d	p_{tukey}	
young IN	young PN	7.593	1.276	5.948	0.624	< .001	***
young IN	young NN	29.403	1.266	23.231	2.418	< .001	***
young PN	young NN	21.81	0.721	30.252	1.793	< .001	***
early old IN	early old PN	17.191	1.391	12.362	1.414	< .001	***
early old IN	early old NN	30.189	1.352	22.333	2.482	< .001	***
early old PN	early old NN	12.998	0.762	17.066	1.069	< .001	***

Note. Results are averaged over the levels of: area

Note. P-value adjusted for comparing a family of 6, only relevant comparisons shown

*** p < .001

Table 5.2

Post Hoc Comparisons - age_bracket ∗ Cell-type ∗ area

		Mean Diff	SE	t	Cohen's d	p_{tukey}	
young IN M1	young PN M1	6.422	1.891	3.396	0.528	0.034	*
young IN M1	young NN M1	29.677	1.872	15.854	2.44	< .001	***
young PN M1	young NN M1	23.255	1.079	21.549	1.912	< .001	***
young IN S1	young PN S1	8.764	1.715	5.111	0.721	< .001	***
young IN S1	young NN S1	29.129	1.704	17.094	2.395	< .001	***
young PN S1	young NN S1	20.366	0.956	21.297	1.675	< .001	***
early old IN M1	early old PN M1	18.541	1.997	9.282	1.525	< .001	***
early old IN M1	early old NN M1	28.156	1.945	14.474	2.315	< .001	***
early old PN M1	early old NN M1	9.615	1.159	8.296	0.791	< .001	***
early old IN S1	early old PN S1	15.842	1.935	8.185	1.303	< .001	***
early old IN S1	early old NN S1	32.222	1.878	17.162	2.649	< .001	***
early old PN S1	early old NN S1	16.38	0.988	16.571	1.347	< .001	***

Note. P-value adjusted for comparing a family of 12, only relevant comparisons shown

* p < .05, ** p < .01, *** p < .001